




Cite this: *RSC Adv.*, 2024, 14, 38426

Versatile photocatalytic activities of indenoquinoxalines for dye reduction, single-crystal nucleation, and MNP formation with iron scrap under sunlight†

Renu Kumari  and Man Singh *

In this work, 11*H*-indeno[1,2-*b*]quinoxalin-11-one (IQ), 7-nitro-11*H*-indeno[1,2-*b*]quinoxalin-11-one (NIQ), and 7-chloro-11*H*-indeno[1,2-*b*]quinoxalin-11-one (CIQ) as indenoquinoxalines (IQPs) and 7-nitro-2'-(4-nitrophenyl)-5',6',7',7a'-tetrahydrospiro[indeno[1,2-*b*]quinoxaline-11,3'-pyrrolizine]-1',1'(2'*H*)-dicarbonitrile (SIQPNO₂) spiroheterocyclics were synthesized. These molecules photocatalytically reduced methylene blue (MB), methyl orange (MO), brilliant blue R (BBR), and Rhodamine B (RhB) in aqueous acetonitrile (aq-ACN) under sunlight (SL) for the first time. The IQPs and SIQPNO₂ with a lanthanide graphene oxide template (LGT) of lanthanide sulfide nanorods (Ln₂S₃, Ce₂S₃, Tb₂S₃, and Ho₂S₃) photocatalytically reduced the dyes. IQ alone reduced MB in ~2 min, while with LaGT, CeGT, TbGT, and HoGT in 7, 10, 11, and 13 min, respectively. NIQ and CIQ alone photocatalytically reduced MB in 18 and 32 min, while with LaGT, CeGT, TbGT, and HoGT in 18, 31, 23, and 28 min and 33, 55, 45, and 51 min, respectively. IQ with CO₂ photocatalytically reduced MB and QHIn in 90 s and 17 min unlike 2 and 24 min without CO₂, respectively. SIQPNO₂ alone reduced MB in 190 min, while with CeGT, TbGT, HoGT, and LaGT in 242, 225, 197, and 88 min, respectively. IQ with LaGT photocatalytically reduced MB in 7 min, while SIQPNO₂ with LaGT in 88 min. IQ received maximum photon (*hν*) producing robust redox cycles (ROCs) compared to SIQPNO₂. SIQPI, SIQPII, SIQPIII, and SIQPNO₂ (SIQPs) individually reduced MB in 95, 43, 54, and 190 min, while SIQPs with NIQ in 63, 35, 47, and 64 min, respectively. IQ with Fe scrap in ACN developed a single crystal in 2 weeks, while in 2 : 8, 3 : 7, 5 : 5, 7 : 3, and 8 : 2 aq-ACN media, the magnetic nanoparticles (MNPs) developed at normal temperature and pressure (NTP).

Received 2nd July 2024
Accepted 14th August 2024

DOI: 10.1039/d4ra04808c

rsc.li/rsc-advances

Introduction

Brugnatelli in 1818, Dobereiner in 1832, Runge in 1834, Friedlander in 1906, Treibs in 1936, Chargaff in 1951, and others have synthesised and developed heterocyclic compounds with medicinal applications.^{1,2} Consequently, diverse heterocyclic molecules have found applications in biological fields, cosmetics, drug designing, and dye synthesis. However, to date, no scientist has delved into their potential for interfacing with solar radiation to induce electronic transitions for photocatalytic reduction (PCR) studies. Their active surfaces facilitate their use as robust photocatalysts for reducing effluents but no study has been reported yet. In this regard, our previous studies with SIQPI, SIQPII, and SIQPIII³ demonstrated novel science with a chiral carbon atom (CCA) equipartitioning eigenenergies of each constituent for generating single-valued wavefunctions on receiving *hν*. SIQPI, SIQPII, and

SIQPIII³ explored in our previous research, demonstrating an efficacy for reducing dyes and persistent pollutants, have inspired further investigation into heterocyclic NIQ as a base unit of SIQPs in studying its energy-storing capabilities for potential applications in the PCR. Various photocatalysts are being reported to photodegrade both industrial and biological effluents, often taking a longer time. Many researchers have failed to elucidate the role of eigenenergies in analysing the photocatalytic activity, leaving a crucial aspect unexplored. Except IQPs, no heterocyclics have been reported as photocatalysts for reducing a waste dye. It has created a basis for studying IQPs in PCR, apart from SIQPs, based on eigenenergies.³ IQPs have developed ROCs by overcoming a quantum energy barrier (QEB) on lowering the band gap to photocatalytically reduce the dyes. The IQPs compared to SIQPs have investigated the role of CCA for enhancing the functionality *via* Förster resonance energy transfer (FRET).³ In our previously reported study, SIQPs have successfully reduced quinonoid phenolphthalein (QHIn).³ The IQPs have reduced the dyes in 1/6th time shorter than SIQPNO₂. The PCR process, UV-Vis transition, quantum yield (Φ), single crystal with Fe scrap, and MNPs⁴ with aq-ACN indicate robust photochemical activities of IQPs having both

Central University of Gujarat, Gandhinagar, India. E-mail: renukumaribalot6@gmail.com; mansingh50@hotmail.com; Tel: +91-079-23260076; +91-079-23260210

† Electronic supplementary information (ESI). See DOI: <https://doi.org/10.1039/d4ra04808c>



electron-withdrawing groups (EWGs) and electron-releasing groups (ERGs). NIQ, a base matrix of SIQPs, has demonstrated a reduced dye reduction time; this inspired the synthesis of SIQPNO₂, with two terminal NO₂ functional group (FG), by condensing NIQ with 2-(4-nitrobenzylidene) malononitrile using L-proline in ACN. Moreover, NIQ with SIQPs has acted as a photocatalyst to reduce dyes. The eigenenergies of NIQ and SIQPs were mutually elevated valence bands (VBs) to conduction bands (CBs) instead of synthesizing new photocatalysts. The ERG and EWG of IQPs have simulated the eigenenergies, for example, SIQPs with NIQ have reduced MB⁵ in 43–190 min unlike alone NIQ in 12 min respectively. IQPs and SIQPs generate the positive and negative (h⁺) and (e⁻) holes in the same phase to photocatalytically reduce dyes in a shorter time. Moreover, their physicochemical properties have assessed a role of solvent with IQPs, SIQPNO₂, SIQPNO₂ + NIQ, SIQPI + NIQ, SIQPII + NIQ, and SIQPIII + NIQ for dye reduction, which are not reported yet and explored in this paper.^{6–12} IQPs and SIQPNO₂ (ref. 13–17) are also studied with LaGT (La³⁺ = 4f⁰), CeGT (Ce³⁺ = 4f¹), TbGT (Tb³⁺ = 4f⁸), and HoGT (Ho³⁺ = 4f¹⁰) respectively to photocatalytically reduce dyes followed by adsorption. IQPs + LGT and SIQPNO₂ + LGT, as lanthanide organometallic interphases, have effectively reduced dyes using unpaired 4f^{#e} configurations and never been reported yet. The IQPs and SIQPNO₂ both with LGT do not mutually synchronize under *hν*, interact differently with each constituent and dye by elongating the PCR time. The IQ has influenced Fe rusting in different aq-ACN ratios with a novel substantial study. The electronic configurations of IQPs and SIQPs with NIQ have lowered a QEB. The IQPs and SIQPs with NIQ have reduced the dyes by maintaining in a monodispersed state. As their higher surface energies interact strongly with both the dyes and medium, such photocatalytic activities could be used as an excellent photosensitive solvent, light sensor, photoluminescence, and to monodisperse and reduce persistent pollutants. The ACN has monodispersed SIQPs and IQPs with weaker van der Waals forces without structural split while insoluble in water and unable to photocatalytically reduce the dyes along its robust split. Pure ACN nucleated a single crystal without splitting, whereas 3 : 7 aq ACN induced splitting, forming MNPs along with valuable products on recycling.

Experimental section

Materials

Thin-layer chromatography (TLC) plate, AR-grade hexane (Sigma-Aldrich ≥99%), ethyl acetate (Sigma-Aldrich ≥99%), dichloromethane (DCM) (Sigma-Aldrich ≥99.8%), dimethylformamide (DMF) (Sigma-Aldrich ≥99.8%), acetone (Sigma-Aldrich ≥99.9%), MeOH (Sigma-Aldrich ≥99.9%), and ACN (Sigma-Aldrich ≥99.8%) were used. Para-nitro benzaldehyde, ninhydrin, malononitrile, lithium bromide (LiBr), acetic acid (CH₃COOH), methanol (CH₃OH), L-proline, magnetic beads, and Whatman filter paper were used as received.

Characterization methods

Structures were analyzed by ¹H and ¹³C NMR (500 MHz, Bruker Avance Spectrometer) in CDCl₃ at 500 and 125 MHz using TMS

internal standard, mass spectra using an Agilent Technology 6545 Q-TOF LC-MS spectrometer at 70 eV, FT-IR spectra from 200–800 cm⁻¹ with KBr pellets using a PerkinElmer TL8000 TG-IR interface, UV-Vis spectra from 190–1100 nm using a UV-1800 SHIMADZU (UV Spectrophotometer) in ESI mode, X-ray diffraction (XRD, powder/single), thermal gravimetric analysis (TGA) using an intercooler PerkinElmer TGA-6000 thermometer for ~25 to 500 °C, high-resolution transmission electron microscopy (HR-TEM) using a JEOL JEM-2100 electron microscope at 200 kV operating voltage, scanning electron microscopy (SEM), stereomicroscopy, atomic force microscopy (AFM, Multimode Scanning Probe Microscope, Bruker), fluorescent spectroscopy (RF-6000 Spectro Fluorophotometer, SHIMADZU CORP), Raman spectroscopy, and elemental analysis.

Synthesis of starting material: synthesis of IQ

Scheme S1:† benzene-1,2-diamine (11 mmol, 1.1 eq., 1.1 g) and ninhydrin (10 mmol, 1.0 eq., 1.8 g) were stirred in CH₃COOH (10 mL) and CH₃OH (30 mL) for 30 min at RT monitored by TLC (Table S1†). A light yellowish product was filtered, washed with CH₃OH, and dried in vacuum, and the structures were investigated by ¹H, ¹³C NMR, and mass analysis (Fig. S1†).

Synthesis of NIQ

Scheme S2:† 4-nitrobenzene-1,2-diamine (11 mmol, 1.1 eq., 1.7 g) and ninhydrin (10 mmol, 1.0 eq., 1.8 g) were stirred in CH₃COOH (10 mL) and CH₃OH (30 mL) for 30 min at RT and monitored by TLC (Table S2†).¹⁸ A yellow product was filtered, washed with CH₃OH and dried in vacuum. The structures were investigated by ¹H, ¹³C NMR, and mass analysis (Fig. S2†).¹⁸

Synthesis of CIQ

Scheme S3:† 4-chlorobenzene-1,2-diamine (11 mmol, 1.1 eq., 1.5 g) and ninhydrin (10 mmol, 1.0 eq., 1.8 g) were stirred in CH₃COOH (10 mL) and CH₃OH (30 mL) for 30 min at RT monitored by TLC (Table S3†). A pale yellow product was filtered, washed with CH₃OH and chilled water, and dried in vacuum, and the structures were investigated by ¹H, ¹³C NMR, and mass analysis (Fig. S3†).

Reaction scaling of SIQPNO₂ synthesis

Scheme S4:† 2-(4-nitrobenzylidene)malononitrile from 4-nitrobenzaldehyde and malononitrile in DMF with LiBr were synthesized (Table S4†). LiBr catalyzed a reaction by rearranging a dispersion phase of 4-nitrobenzaldehyde with malononitrile in DMF (Fig. S4†).

Synthesis of SIQPNO₂

For Scheme S5,† 2-(4-nitrobenzylidene)malononitrile (1.0 mmol, 1.0 eq., 154.5 g) (Table S5†), was separately added to NIQ (1.0 mmol, 1.0 eq., 277 g) and L-proline (1.0 mmol, 1.0 eq., 126.5 g) in ACN (15 mL). Reacting mixtures were stirred and refluxed for 3 h monitored by TLC and visualized with UV-Vis light and iodine. Excess solvent was removed using a rota evaporator. The crude product was washed with DCM and lime water (~3 times)



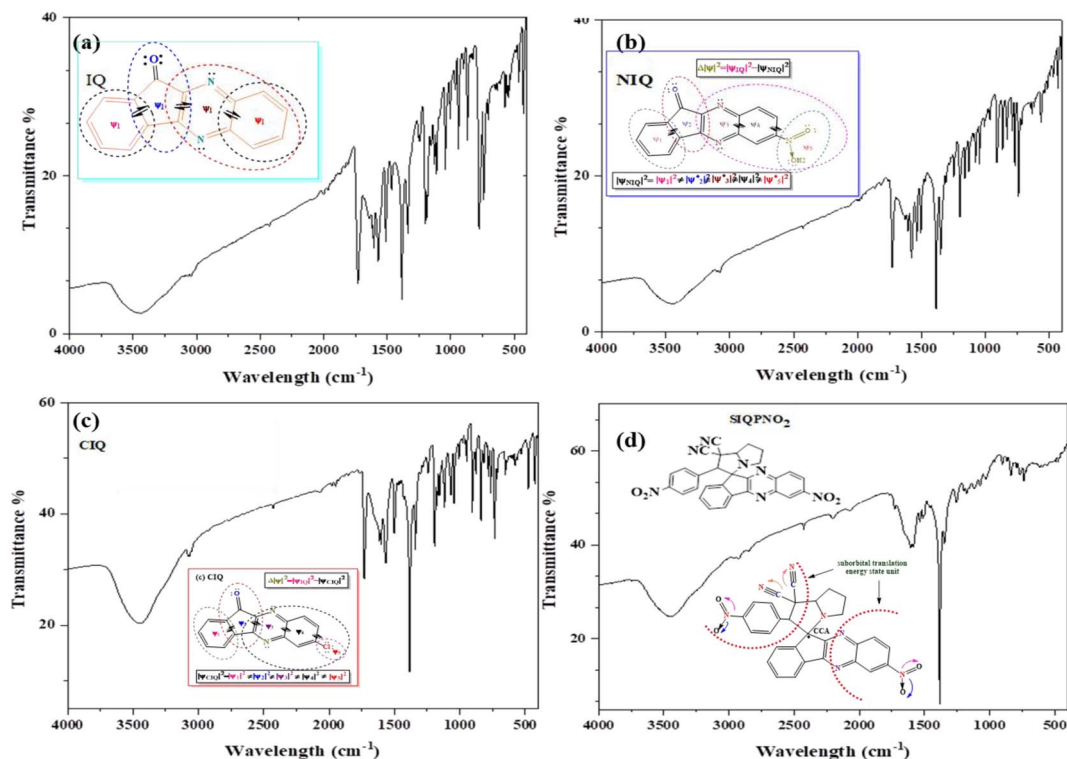


Fig. 1 FT-IR spectra for stretching and bending of (a) IQ, (b) NIQ, (c) CIQ, and (d) SIQPNO₂.

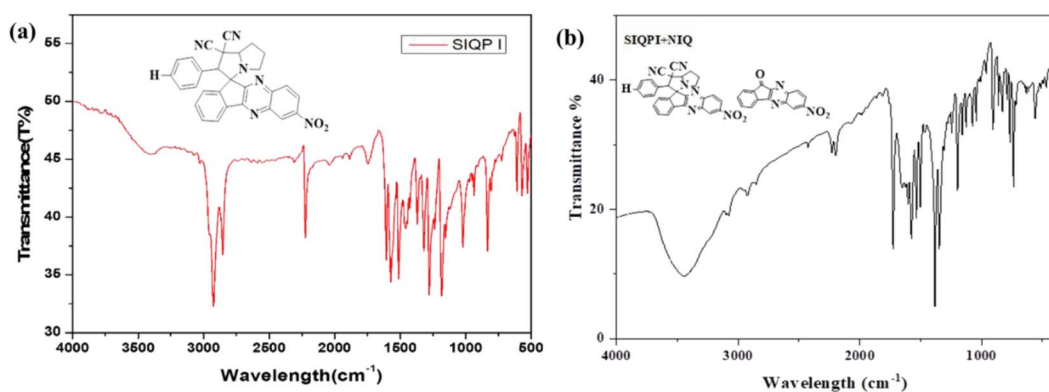


Fig. 2 FT-IR spectra for stretching and bending (a) SIQPI alone (b) SIQPI + NIQ.

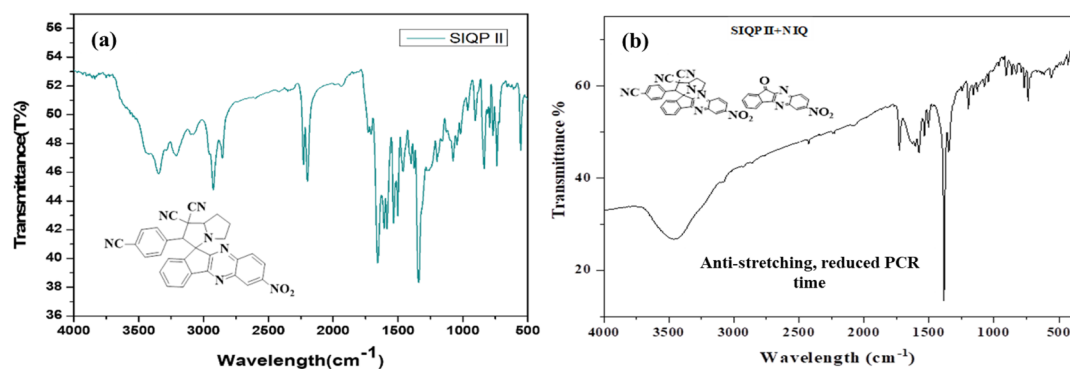


Fig. 3 FT-IR spectra for stretching and bending (a) SIQPII alone and (b) SIQPII + NIQ.



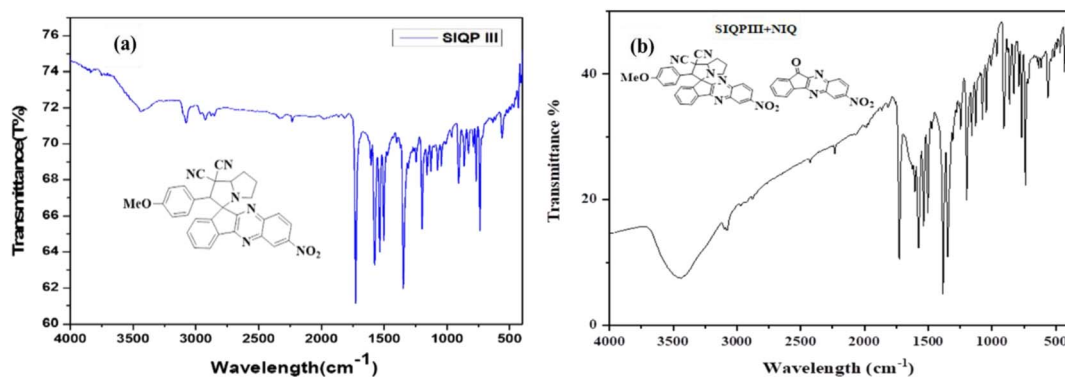


Fig. 4 FT-IR spectra for stretching and bending (a) SIQPIII alone and (b) SIQPIII + NIQ.

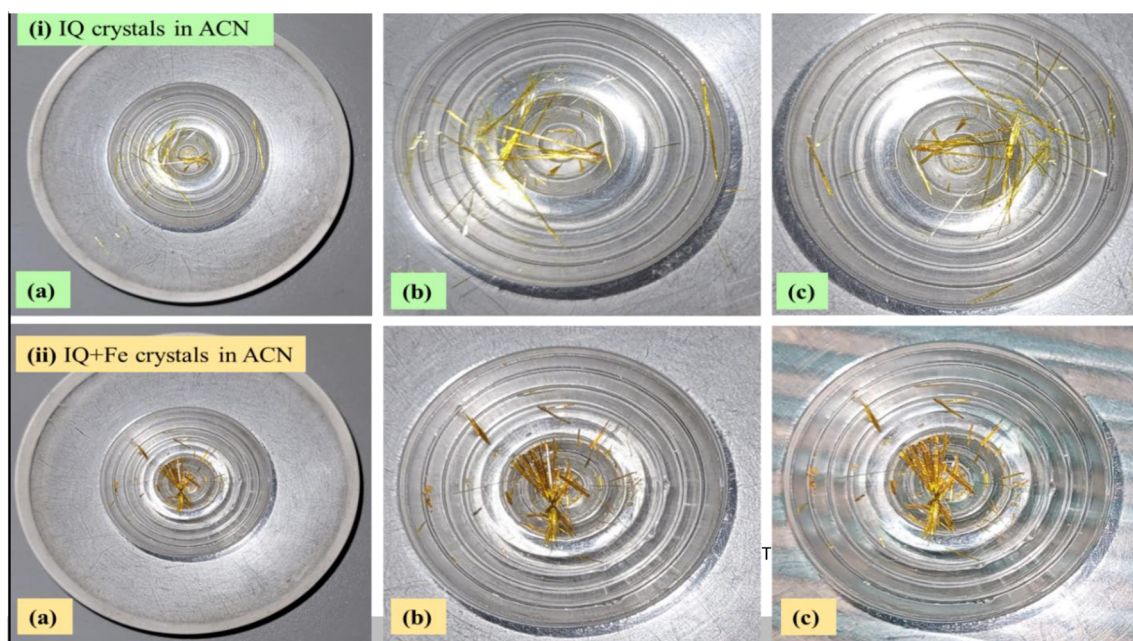


Fig. 5 (i) IQ crystals alone (ii) IQ + Fe crystals in ACN at different magnitude.

to purify by column chromatography (ACME, 60–120 mesh) with 70% petroleum ether + 30% ethyl acetate (EA) eluting mixture, dried under vacuum, and analysed by ^1H , ^{13}C NMR, and mass spectroscopy (Fig. S5a and b †). IQ, NIQ, CIQ, and SIQPNO₂ obtained from Schemes S1–S5 † were characterised by ^1H , ^{13}C NMR spectroscopy, FT-IR spectroscopy, and TGA (Fig. 1). Scheme S6 † infers SIQPI + NIQ (Fig. 2, S6a and b †), Scheme S7 † infers SIQPII + NIQ (Fig. 3, S7a and b †), and Scheme S8 † infers SIQPIII + NIQ (Fig. 4, S8a and b †).

Synthesis of single crystals (model: D8 QUEST, Bruker)

First, 0.001 (M) IQ with Fe scrap of 1.199 g in 5 mL of ACN in vial developed a single crystal of 95.09 mg in two weeks. The single crystal was characterized by XRD and few parameters with single-crystal XRD to obtain a contribution of Fe scrap on IQ

nucleation. Robust crystals are developed by IQ with Fe than IQ alone in ACN (Fig. 5).

Results and discussion

^1H , ^{13}C NMR, and FT-IR

Two separate doublets in ^1H NMR spectra of SIQPNO₂ confirm a pyrrolizidine (pyz) ring and multiplets at δ 4.95 ppm (d, 1H, J = 5.5 Hz) pyz NCH proton. The pyz proton attached to a phenyl ring is deshielded at δ = 4.81 (d, 1H, J = 5.8) and multiplets at δ 7.49–10.16 ppm for aromatic protons (Fig. S5a †) and also confirmed by ^{13}C NMR (Fig. S5b †). NIQ having EWG NO₂ has deshielded the H atoms by attracting the density of energy state (DOS) of double bonds for robust ROCs reducing dyes in a shorter time than CIQ. IQPs with NO₂ (EWG) and Cl[−] (ERG)

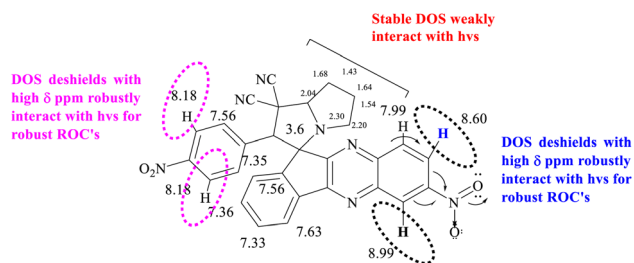


Fig. 6 NO₂ deshielding effect on neighbouring H atom.

have equipartitioned the DOS of π bonds from the VB to the CB to photocatalytically reduce the dyes in a shorter time. No researcher has taken a note of DOS for π bonds, which enhance a Fermi sphere to expedite photocatalyzing holes supported by the deshielding effect, noted in ¹H NMR. The CCA avoids DOS intermixing of EWG and ERG by minimizing the undesired collisions influencing PCR. However, deshielding and shielding

of π bond with ¹H NMR for receiving $h\nu$ have never been correlated with PCR. The deshielding of π bonds shortened a PCR time with photocatalysts as a novel breakthrough, it could be applied in various fields (Fig. 6).

Moreover, the quantum energy equilibrating the DOS with nearly residual surface energy to respond under $h\nu$ has never surfaced in PCR. The IQPs and SIQPs acted as rigid harmonic oscillators to synchronize the residual surface energies. Moreover, it elucidates the nature of photocatalysts acting as 1D potential energy (PE) systems with few quantum energies denoted as synchronized residual energy to a single phase. The quantum resonating energies respond to SL generating ROCs as $\psi_1, \psi_2, \psi_3, \psi_4$, and ψ_5 of IQPs and SIQPNNO₂ via FRET. IR stretching and bending frequencies at ~ 1600 – 1550 and 2260 cm⁻¹ infer –NO₂ and –C \equiv N in NIQ and SIQPNNO₂. Moreover, at 1745 – 1715 cm⁻¹ infers C=O and C–Cl while at 850 – 550 cm⁻¹ the ketonic C=O and Cl in IQPs. The strong band at 800 – 850 cm⁻¹ appeared for a 1,4-disubstituted aromatic ring for SIQPNNO₂.

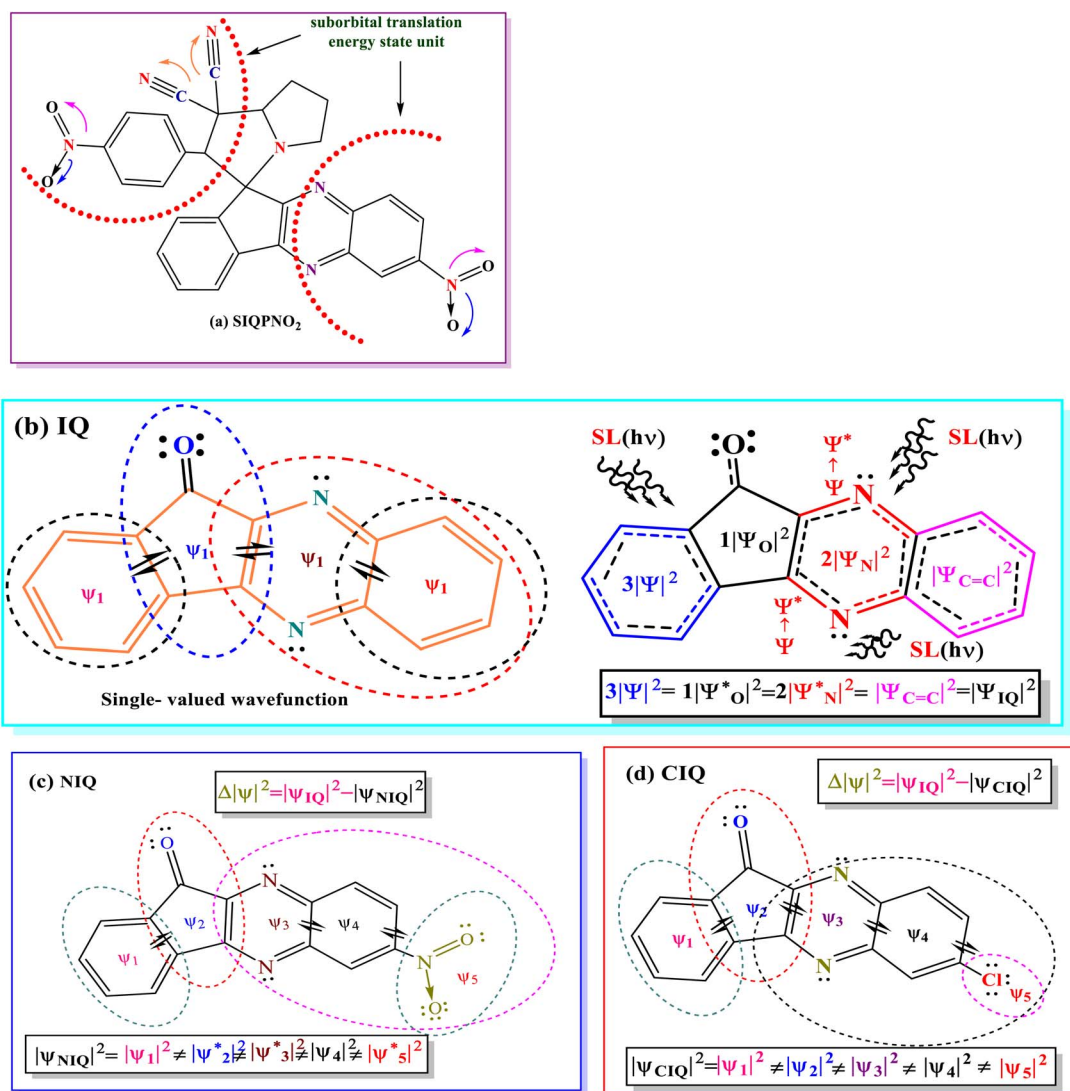


Fig. 7 Functional domains of (a) SIQPNNO₂, (b) IQ, (c) NIQ, and (d) CIQ.



FT-IR spectra of IQPs and SIQPs with NIQ to photocatalytically reduce dyes

Electronically, IQ stretches as the 1st order, unlike NIQ with NO₂ and CIQ with Cl that slightly weaken the stretching with high intensities. The holes of IQ in a single phase, unlike NIQ and CIQ at higher intensities with EWG and ERG, shorten the PCR time. IQ broadened a peak of C–C bond from 2200 to 3500 cm^{−1} on aligning the charges unlike with the NO₂ and Cl stretching differently. The CIQ with ERG resonates that the π conjugation increased the stretching in the same phase with sharper peaks in the 400–1200 cm^{−1} fingerprint region. The NIQ gains an integrated π conjugation intensifying IR transmittance. The DOS¹⁹ of NIQ linearly aligns stretching *vis-à-vis* conjugation. The C–C bonds are equipartitioned, leading to 6.7% min^{−1} PCR rate for MB. The CIQ with sharpened stretching unlike IQ with a least C–C stretching photocatalytically reduced MB in 2 min, whereas NIQ has weakened DOS due to electron–electron repulsion (EER) (Fig. 7). The π electron cloud of NIQ stretches in a fingerprint region and used with SIQPs as a cophotocatalyst *via* mutually monodispersion for receiving the *hν*. IR of SIQPI + NIQ having FP aligned with NIQ *via* C=C bonds has sharpened a stretching to photocatalytically reduce MB in 63 unlike 95 min with SIQPI alone (Fig. 7). The SIQPII + NIQ has also weakened stretching at 2200–400 cm^{−1} for CN intensifying the fingerprint region. SIQPII + NIQ with 3500–2000 cm^{−1} as IR active has reduced MB in 35, unlike 43 min with SIQPII alone. SIQPIII + NIQ from 1500 to 4000 cm^{−1} strengthened the unspent resonating sites generating a maximum stretching as IR active with a shorter PCR time than SIQPIII alone. Manifold intensities inhibited by SIQPIII + NIQ photocatalytically reduced MB in 47 min, unlike 54 with SIQPIII alone.¹⁸ The SIQPs under SL have reduced dyes in our earlier study¹⁸ and are extended now with IQPs. The wavefunctions of IQPs, SIQPs, and SIQPs + NIQ with EWG and ERG using solvation energies as a communicating FRET accessed to the dyes. The 3 : 7 aq-ACN with $\pi \rightarrow \pi^*$ and $n \rightarrow n^*$ have quantized a photocatalytic chemistry to lay down a 2nd-generation photocatalysis. The IQPs and SIQPs with NIQ have reduced dyes in a shorter time due to single-valued wavefunctions (Fig. 7, Chart 1(a and b)). SIQPNO₂ alone with enormous $\pi \rightarrow \pi^*$ and $n \rightarrow n^*$ has reduced MB in 2.16 times shorter period than with LGT. The 4f^{ne} electrons of lanthanides of LGT seem to interrupt the hole generation²⁰ (Fig. 8). The *hν* excites enormous π and lone pair of electrons (LPE) of SIQPNO₂ that photocatalytically reduce an MB philicphobic medium in 190 min, and such studies have not been reported previously. NIQ has reduced the dyes in a shorter time with SIQPI, II, III, and SIQPNO₂ than SIQPI, II, and III alone¹⁸ due to the same phase ROCs.²¹ IQ with π conjugation and LPE of O and N atoms have produced holes in the same phase to photocatalytically reduce in 2 min. NIQ with NO₂ and CIQ with Cl have enhanced PCR time unlike IQ. IQPs with LGT have reduced dyes in longer time while the SIQPs with NIQ and LGT in shorter and longer PCR times respectively. The LaGT, CeGT, TbGT, and HoGT compared to Ln₂S₃, Ce₂S₃, Tb₂S₃, and

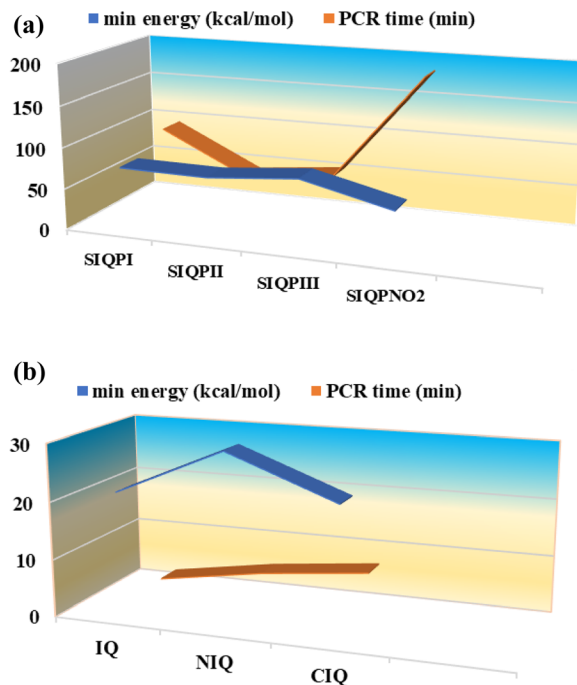


Chart 1 (a) SIQPs and (b) IQPs vs. PCR time (min) and minimum energies (kcal mol^{−1}).

Ho₂S₃ LSNR respectively have shortened a dye PCR time. The $\pi \rightarrow \pi^*$ and 4f^{ne} \rightarrow 4f^{ne*} of LGT could not compete the $\pi \rightarrow \pi^*$ of IQPs, as alone LGT has reduced MB in 64 min than 2 with alone IQ, LGT with IQPs in 10–55 min ($\psi_{\pi} \rightarrow \pi - \psi_{4f^{ne}} \rightarrow 4f^{ne*}$). IQPs + LGT with $\pi \rightarrow \pi^*$ and 4f^{ne} \rightarrow 4f^{ne*} have shortened the MB PCR time than our reported studies. LGT with infinite π conjugation aligns at a periphery of IQPs intensifying π conjugation *via* FRET for MB PCR. The $\pi \rightarrow \pi^*$ and 4f^{ne} \rightarrow 4f^{ne*} of LGT align with $\pi \rightarrow \pi^*$ and $n \rightarrow n^*$ of IQPs reducing dyes in a shorter time. The IQPs with LGT have generated IQPs + LGT. IQPs alone after MB reduction remained monodispersed resulting in a transparent nanoemulsion as thin films suitable to be used in paint industries and antireflecting coating agents.²²

While LGT with IQPs that photocatalytically reduced MB settled as a black coloured nanocluster, IQPs and SIQPs alone yielded a transparent nanoemulsion (Fig. 8). The π conjugation and 4f^{ne} of LGT with IQPs photocatalytically reduced MB in a longer time than IQPs alone on stronger inter and intra π interactions. IQPs with LGT after MB PCR did not interact with the medium as IQP + LGT have adsorbed a leuco MB (LMB) than alone IQPs (Fig. 8). Compared to 43% min^{−1} with IQ, NIQ and CIQ have lowered PCR MB rates by 6.7 and 2.2% min^{−1}. NIQ photocatalytically reduced MB in 12 min while the NIQ with SIQPI, II, III and SIQPNO₂ in 63, 35, 47, and 64 min respectively. The NIQ adhered with SIQPs with a higher friccohesity²³ acted as cophotocatalyst with eigenenergies as SIQPI + NIQ > NIQ in 63 > 12 min to photocatalytically reduce MB respectively. Therefore, NIQ has lowered the PCR time by 34% *via* enormous 2n \rightarrow 2n* and $\pi \rightarrow \pi^*$ of >O unlike SIQPs alone. NIQ with SIQPs has reduced the PCR time from 95 to 43 min as >O with 2



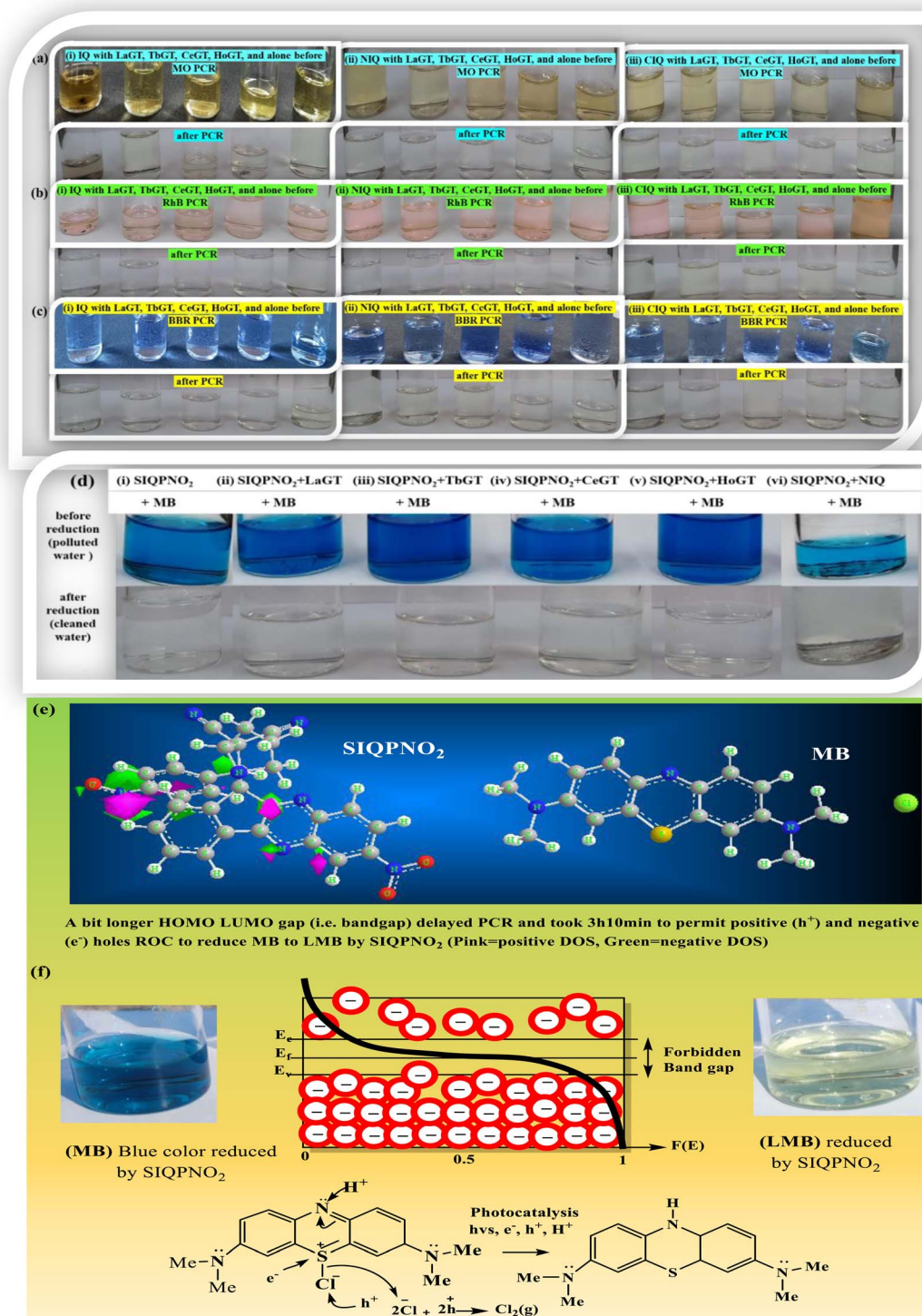


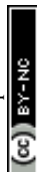
Fig. 8 Photocatalysis of MO, RhB, BBR by (a) IQ, (b) NIQ, (c) CIQ each with LGT and MB PCR by (d) SIQPNO₂ alone, with LGT, and NIQ, (e) molecular orbital electronic charge DOS of SIQPNO₂ and MB and (f) band gap mechanism to reduce MB by SIQPNO₂.

LPE and π of NIQ on $2n \rightarrow 2n^*$ and $\pi \rightarrow \pi^*$ synchronizing the and $4\pi \rightarrow 4\pi^*$ of 2 ($-C\equiv N$) of pyz with SIQPs along with its NO₂ (Fig. 9). Alone NIQ with >O PCR in 12 min but >O FG with SIQPs via CCA reducing dye in 95 min. The NIQ with SIQPs has generated DOS by minimizing the interference of mutual DOS of pyz and free phenyl (FP) to photocatalytically reduce dyes

expeditiously. SIQPs + NIQ with a higher surface energy overcome QEB to PCR pollutants in a shorter time (Fig. 9).²⁴

UV-vis spectral analysis

UV-Vis maximum absorptions (λ_{\max}) for IQ, NIQ, and CIQ are at 292, 278, and 293 nm respectively, while for SIQPNO₂ at 278 and



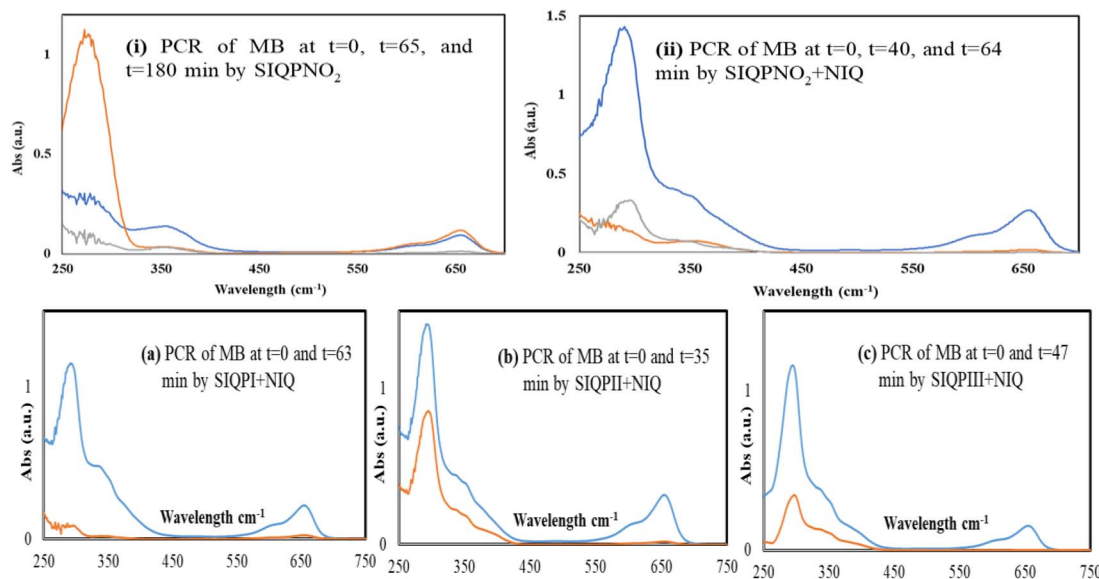


Fig. 9 UV-Vis for MB reduction using (i) SIQPNO₂ and (ii) SIQPNO₂ + NIQ, (a) SIQPI + NIQ, (b) SIQPPII + NIQ, and (c) SIQPPIII + NIQ.

375 nm. Molar absorption coefficients (ϵ_{\max}) were calculated from them (Fig. 10(a–d)). Longer λ_{\max} infers less collision shortening the PCR time. The ϵ_{\max} values for IQ, NIQ, CIQ, and SIQPNO₂ are 199, 266, 406, and 533 M⁻¹ cm⁻¹ with the PCR time as SIQPNO₂ > CIQ > NIQ > IQ for MB respectively. IQ with the lowest ϵ_{\max} without ERG or EWG synchronizes eigenenergy to photocatalytically reduce MB in a shorter time. IQPs and

SIQPNO₂ could have synchronized the eigenenergies from one to another atom on entropic disorders (ΔS) favourably aligning the h^+ and e^- holes with $\Delta S > 0 < \Delta G$ Gibbs free (ΔG) and activation energy (E_a) (Fig. 10 and 11).²⁵ Enthalpy (ΔH) in the PCR process has generated entropy to reorient the photocatalysts and dyes like IQ in the same phase. The $h\nu$ from solar radiation could have mildly excited $4n \rightarrow 4n^*$ and $8\pi \rightarrow 8\pi^*$ of

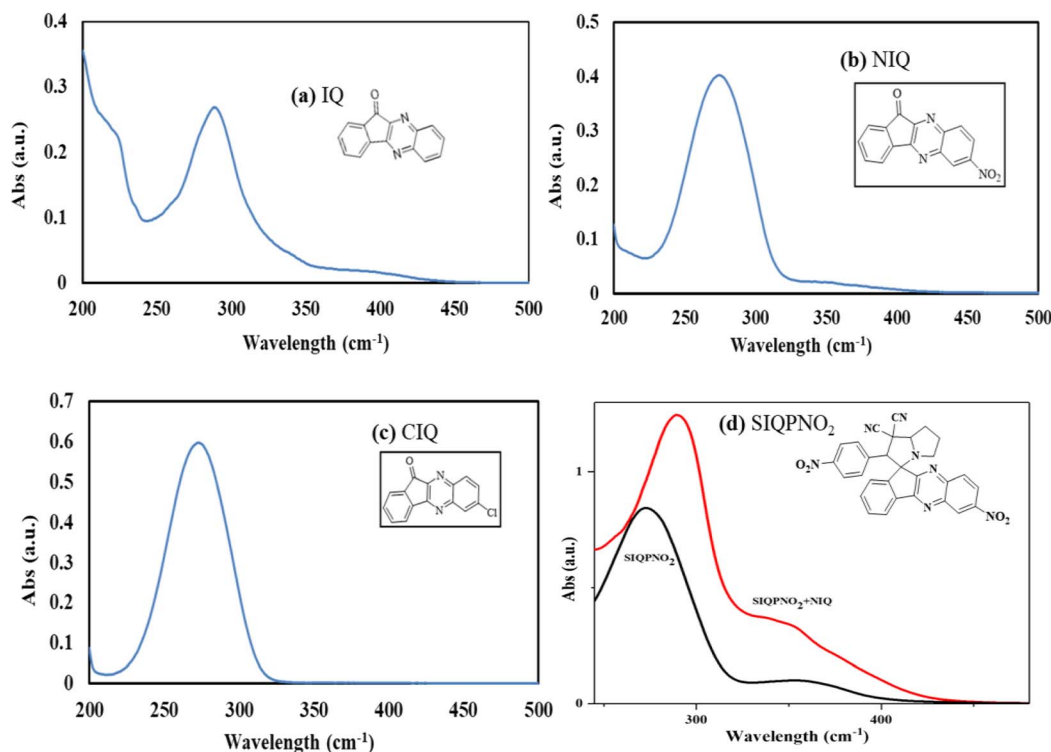


Fig. 10 UV-Vis absorption (a) IQ, (b) NIQ, (c) CIQ, and (d) SIQPNO₂ and SIQPNO₂ + NIQ.

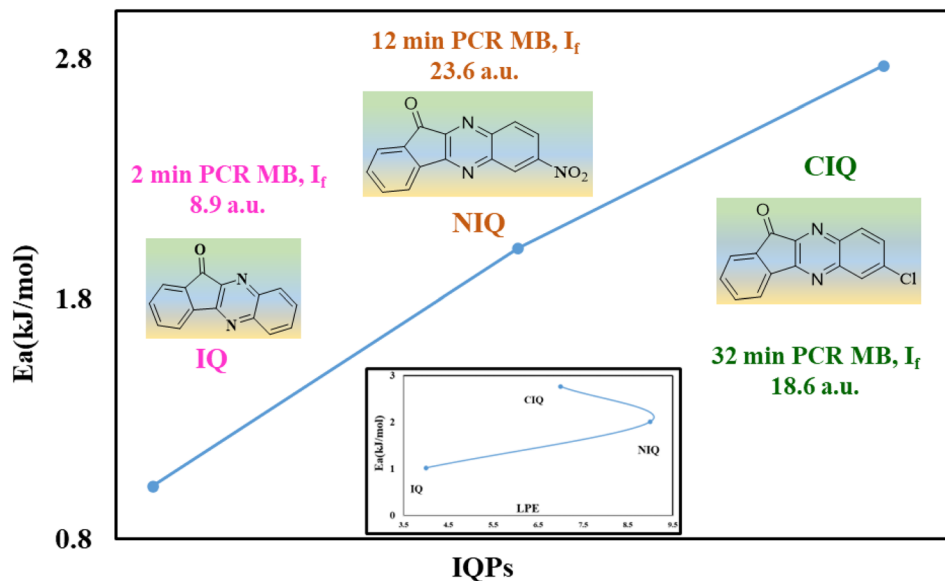


Fig. 11 Plot of E_a and LPE vs. IQPs.

IQ via intra-FRET mechanism (Fig. 12). The $4n \rightarrow 4n^*$ and $8\pi \rightarrow 8\pi^*$ indistinguishable energy levels of IQ have synchronized the wavefunctions fitted with time-dependent Schrödinger equation: $1.41\psi_{IQPs} = (\phi_{4n^*} \pm \phi_{8\pi^*})$.²⁶ PCR normalizes as $\psi_{IQ} = N^2 \int_{-\infty}^{\infty} |\psi(x, y, z)|^2 dx = 1$, $= N^2 \int \psi^* \psi dx = 1$ with IQ while with NIQ and CIQ, partial orthogonal activity is depicted as eqn (1)–(3).

$$\psi_{NIQ/CIQ} = \int_{-\infty}^{\infty} |\psi(x, y, z)|^2 dx = 0 \text{ or } \int \psi_m^* \psi_n d\tau = 0, \quad (1)$$

$$E_{IQ} = \int_{-\infty}^{\infty} \phi_m^* \phi_n dx = \delta_{nm} = 1, \text{ if } m = n \quad (2)$$

$$E_{NIQ/CIQ} = \int_{-\infty}^{\infty} \phi_m^* \phi_n dx = \delta_{nm} < 1, \text{ if } m \neq n \quad (3)$$

The m and n eigenenergy coefficients of wavefunctions infer a constructive interference with IQ (Fig. 12).²⁷ While the NIQ and CIQ as $|\psi_{IQ}| \pm |\psi_{NIQ/CIQ}| < 1$ as $|\% \psi_{IQ}| \pm |\% \psi_{NIQ}|$ reduced in 12 and $|\% \psi_{IQ}| \pm |\% \psi_{CIQ}|$ in 32 min to photocatalytically reduce MB (Fig. 12 and S9–S10†). The orientation of wavefunction ($\phi_{4n^*} \pm \phi_{8\pi^*}$) decides PCR where IQ with synchronized $\psi_{IQ} = 0.71(\phi_{4n^*} \pm \phi_{8\pi^*})$ PCR in 2 min unlike 32 and 12 min with partially orthogonal $\psi_{NIQ} = 0.71((\phi_{4n^*} \pm \phi_{8\pi^*}) - (\phi_{5n^*} \pm \phi_{1\pi^*}))$ and $\psi_{CIQ} = 0.71((\phi_{4n^*} \pm \phi_{8\pi^*}) - (\phi_{3n^*}))$ for CIQ and NIQ respectively (Fig. 12). IQ generates the holes of α and β energy state coefficients from HOMO \rightarrow LUMO in the same phase with $\phi_{4n^*} \pm \phi_{8\pi^*}$ differing from NIQ $\phi_{5n^*} \pm \phi_{1\pi^*}$ and CIQ (ϕ_{3n^*}) as intrinsic disintegrating eigenenergies.²⁸ Such pioneering quantum mechanics ascertains a role of ERG for MB PCR in 32 and EWG in 12 min as phase-dependent reduction of effluents (Fig. S9 and S10†). The IQ receives the $h\nu$ at the same rate at which the eigenenergies of O and 2N atoms synchronize the hole without hurdling the $h\nu$ receptance, unlike CIQ and NIQ with different α and β quantum

states. IQ with localised α to β states in HOMO \rightarrow LUMO transition, exhibits wavefunctions $\psi_1 \neq \psi_1 \neq \psi_1 \neq \psi_1 \neq \psi_1$ without causing undesired electron–electron collisions (EEC) or Lorentz activities, resulting in a least E_a .²⁹ The ERG and EWG of CIQ and NIQ could have generated ($\psi_1 \neq \psi_2 \neq \psi_3 \neq \psi_4 \neq \psi_5$) α to β quantum states, unlike ($\psi_1 = \psi_1 = \psi_1 = \psi_1 = \psi_1$) α to β with IQ respectively. The common α_o and β_o energy coefficients of O atom in IQPs orientated differently to explain an extended conjugation and realigning mechanism. For example, IQ has reduced dye in 2 min, as the wavefunctions of ketonic O ($\psi_{>CO}$) also receive $h\nu$ at the same rate as other constituents of IQ, without any delay in localizing the activities. It elucidates the PCR mechanism as $\alpha + \beta$ simulate the wavefunctions as $\psi_s = 0.71(\phi_{4n^*} + \phi_{8\pi^*})$ for HOMO and $\alpha - \beta$ as $\psi_s = 0.71(\phi_{4n^*} - \phi_{8\pi^*})$ for LUMO. The synchronised IQ with wavefunctions $\psi_s = c_{1n}\phi_{1n} + c_{2n}\phi_{2n} + \dots + c_{8\pi}\phi_{8\pi}$ (c is coefficient of ψ and phase (ϕ)) are in single phase with least E_a .

The $4n \rightarrow 4n^*$ could have synchronized $8\pi \rightarrow 8\pi^*$, as 2nd set of eigenenergies aligning $4n$ eigenfunctions + 8π eigenfunctions $\rightarrow 4n^*$ eigenenergies + $8\pi^*$ eigenenergies in the same phase. The PCR of MB in 2 min infers a least scattering of $h\nu$ as IQ with a least E_a resonating the $\lambda_{4n^*} + \lambda_{8\pi^*}$ holes transferred to MB unlike NIQ and CIQ (Fig. 12). The solvent aligning pattern around IQ and dye could have the same zetapotential around $4n$ of N and 8π bonds via quadrant synchronization of $\lambda_{4n^*} + \lambda_{8\pi^*}$ eigenenergies with hole intensities $I_r = (a_{4n^*})^2 + (a_{8\pi^*})^2$. The λ_{4n^*} & $\lambda_{8\pi^*}$ restricts reorientation to the spatial domain of IQ avoiding EER in PCR. With IQ, the $\phi_m, \phi_n, \phi_o \dots \phi_i$ DOS w.r.t. $\psi_1, \psi_2, \psi_3, \psi_4, \psi_5, \psi_6$, and ψ_7 of a similarly π -conjugated electron system in the box (double bond) on receiving $h\nu$ generated holes to photocatalytically reduce the dye. Their respective wavefunctions equalize the charge-deficient center of dye. IQ without EWG and ERG FG may not orient specific DOS where the $h\nu$ reorient with almost similar energy and angular moments. The



[illegible]

Figure 1 consists of two parts: (a) Energy band diagram and (b) Chemical reaction scheme.

(a) Energy band diagram: The diagram shows the conduction band (CB) and valence band (VB) of a photocatalyst. The CB has a red band labeled [red] and an empty blue band labeled [O]. The VB has an empty blue band labeled [O] and a red band labeled [red]. The LUMO (Lowest Unoccupied Molecular Orbital) is at the top of the CB, and the HOMO (Highest Occupied Molecular Orbital) is at the bottom of the VB. The process is labeled "Hydrolysis step" and "Photocatalysis". The reaction $2\text{H}_2\text{O} = 4\text{H}^+ + 2\text{O}_2$ is shown, with $4\text{H}^+ + 4\text{e}^- = 2\text{H}_2$ and $2\text{O}_2 + 4\text{h}^+ = \text{O}_2$. The overall reaction is $2\text{H}_2\text{O} = 2\text{H}_2 + \text{O}_2$.

(b) Chemical reaction scheme: The scheme shows the photocatalytic mechanism of MB. It starts with MB (Methylene Blue) in its ground state Ψ_g . Upon irradiation with visible light (hvs), MB is excited to a singlet state Ψ_f , which then undergoes intersystem crossing to a triplet state Ψ_d . The triplet state Ψ_d is shown in a dashed box. The triplet state Ψ_d can be quenched by H^+ or Cl^- ions, leading to the formation of $\text{Cl}_2(\text{g})$ and H_2 . The reaction is labeled (i) "single valued Ψ ". The overall reaction is $2\text{Cl}^- + 2\text{h}^+ \rightarrow \text{Cl}_2(\text{g})$. The final product is Leuco MB, which is shown in a dashed box.

reorientation of $\Psi_x, \Psi_i, \Psi_k, \Psi_r, \Psi_s$
& Ψ_y , in different domains where
 $\Psi_x \neq \Psi_i \neq \Psi_k \neq \Psi_r \neq \Psi_s \neq \Psi_y$

The diagram illustrates the chemical structure of a photoconductive polymer, likely a photoconductor for organic photovoltaics. The structure features a central conjugated backbone with various functional groups and wavefunction regions indicated by colored dashed circles and labels.

Chemical Structure Details:

- Central Backbone:** A conjugated system consisting of a central benzene ring connected to two phenyl rings, which are further connected to two nitrogen atoms (N) via methylene groups.
- Left Substituent:** A sulfonate group ($\text{O}=\text{S}(=\text{O})\text{O}^-\text{Na}^+$) attached to a phenyl ring, which is part of a larger structure including a chlorine atom (Cl) and a nitrogen atom (N).
- Right Substituent:** A sulfonate group ($\text{O}=\text{S}(=\text{O})\text{O}^-$) attached to a phenyl ring, which is part of a larger structure including a nitrogen atom (N) and a chlorine atom (Cl).
- Bottom Substituent:** A phenyl ring attached to a nitrogen atom (N) via a methylene group, which is further connected to a phenyl ring with an oxygen atom (O) and a propyl group.

Wavefunction Regions and Labels:

- Ψ_r (purple dashed circle) and Ψ_s (red dashed circle) are located at the top left and top right, respectively.
- Ψ_i (yellow dashed circle) is located on the left side.
- Ψ_k (green dashed circle) is located on the right side.
- Ψ_x (magenta dashed circle) is located in the center.
- Ψ_y (orange dashed circle) is located at the bottom.

Mathematical Expressions:

- $\Psi_x \approx \Psi_y$
- $\Psi_{\text{BBR}} = \Psi_x \times \Psi_y = |\Psi|^2$

Phase Labels:

- $-2\pi/a$ (red dot)
- $-\pi/a$ (white dot)
- π/a (black dot)
- $2\pi/a$ (red dot)

Other Labels:

- hvs (orange wavy arrow)

Fig. 12 Proposed mechanism to PCR dyes by IQPs and SIQPNO₂ under SL.

reorientation of NIQ and CIQ with different DOS does not lie in the same phase. The eigenenergy coefficients α and β from HOMO \rightarrow LUMO for NIQ and CIQ having $E_{\text{NIQ}} = \sum_{i=1}^{n=7} \phi_{\text{IQ}} - \sum_{i=1}^{n=3} \phi_{\text{NO}_2}$ and $E_{\text{CIQ}} = \sum_{i=1}^{n=7} \phi_{\text{IQ}} - \sum_{i=1}^{n=1} \phi_{\text{Cl}}$ differ. Replacing an IQ photocatalyst with NIQ and CIQ has changed a PCR time for MB (Fig. S9 and S10†). The spontaneity for generating the $h\nu$ with the IQ plane favours PCR in least time

unlike with NIQ and CIQ. IQ reduced MB, MO, BBR, and RhB in 2, 5, 7, and 12 min respectively on a mutual reorientation of $h\nu$ receiving electrophilic and nucleophilic sites supporting the least absorption (Fig. 12). The electrophilic and nucleophilic sites of photocatalate and photocatalyst respectively bring them together with integrated eigenenergies at a closer distance (r), where the holes reached to reduce a dye (eqn (4)).

$$\text{FRET} = \frac{(\text{Electrophilic photocatalate site} \times \text{nucleophilic photocatalyst})}{4\pi\epsilon r^2} \quad (4)$$

These $\sum_{i=1}^{n=7} \phi_{\text{IQ}}$ eigenenergies with a single wavefunction (ψ_{IQ} = $0.71(\phi_{4n^*} + \phi_{8\pi^*})$) photocatalytically reduce the MB in less time than MO, BBR, and RhB (Fig. 12 and eqn (5)–(8)) by synchronising as (eqn (5)) follows:

$$\psi_{\text{MB}} = 0.71[(\phi_{2n^*} \pm \phi_{7\pi^*}) - 2(\phi_{2n^*})] \quad (5)$$

$$\psi_{\text{MO}} = 0.71[(\phi_{2n^*} \pm \phi_{7\pi^*}) - (\phi_{8n^*} \pm \phi_{3\pi^*})] \quad (6)$$

$$\psi_{\text{BBR}} = 0.71[(\phi_{2n^*} \pm \phi_{10\pi^*}) - (\phi_{24n^*} \pm \phi_{13\pi^*})] \quad (7)$$

and

$$\psi_{\text{RhB}} = 0.71[(\phi_{4n^*} \pm \phi_{7\pi^*}) - (\phi_{4n^*} \pm \phi_{3\pi^*})] \quad (8)$$

RhB is photocatalytically reduced in >5 times compared to MB due to non-equilibrated additional ψ_a of COOH, aligned differently w.r.t. wavefunction ψ_o causing EER. The wavefunction ψ_a of COOH generated eigenenergies in different planes unlike ψ_o detaining its symmetry during hole generation as $\phi_o - \phi_a$ (eqn (8)). The IQ with differently reorientating dyes seems responsible for a high Φ efficiency of PCR. The various eigenenergy sites of photocatalate facilitate PCR by counterbalancing the distinct electrophilic and nucleophilic electronic sites of dyes. The holes partially equilibrated photocatalysts and dyes for PCR over a longer time. BBR, with synchronised wavefunctions (ψ_x) with an asymmetric electronic structure, was photocatalytically reduced in 7 min unlike MB and MO in 2 and 5 min, respectively (Fig. 12). Symmetric π -conjugated BBR interface with the holes of IQ to mutually equilibrate their oscillations for PCR in longer time than MB and MO (eqn (5)–(8)).

Photocatalytic degree of freedom (F) after dye PCR

Photocatalysts and dye both monodispersed in single-phase favour $h\nu$ receptance while after PCR, a dye is adsorbed with photocatalyst noted as follows:

$$F = C - P + x_i \text{ (degree of freedom } (F) \text{ for dye PCR)} \quad (9)$$

The number of reacting species (C), the P phase, and x_i imply quantum mechanical activities (QMA) to initiate DOS.³⁰ The F infers heat and mechanical energy accompanied in bond breaking or making, affecting photocatalysis in a post-reaction

scenario (eqn (9)). The F streamlines electrons from the VB to the CB as per the Drude and Lorentz model unlike with reacting and non-reacting systems. The F specifies generating holes assisted by medium monodispersion without undergoing any structural changes. The F for PCR was calculated for the first time where the $C = 4$, $P = 1$, and $x_i = 2$ ($h\nu$ and FRET) resulting in $F = 5$ at $dT \geq 0$ and $dP \geq 0$. F highlights a nature of photocatalyst, photocatalate, solvent (aq : ACN), $h\nu$, and FRET. The PCR of MB with IQ releases Cl_2 , resulting in a single-phase solution. The $F = C - P$ works as receiving $h\nu$ and emittance is constant during PCR with $C = 4$ and $P = 1$, resulting in $F = 3$ photocatalyst, $h\nu$, and FRET variables. The F realigns assisting variables (A_v) $h\nu$ and FRET on receiving $h\nu$ continuously for PCR. The IQ remained kinetically and thermodynamically stable with $F = 1$ due to minimum dS in quadrupolar aq : ACN as per Prigogine. The $dG = f(T, P, \text{aq}, \text{ACN}, \text{photocatalyst (lyst)}, \text{photocatalate (late)})$ has initiated as in eqn (10) and (11).

$$dG = \left(\frac{\partial G}{\partial T}\right)dT + \left(\frac{\partial G}{\partial P}\right)dP + \left(\frac{\partial G}{\partial n_{\text{ACN}}}\right)dn_{\text{ACN}} + \left(\frac{\partial G}{\partial n_{\text{H}_2\text{O}}}\right)dn_{\text{H}_2\text{O}} + \left(\frac{\partial G}{\partial n_{\text{lyst}}}\right)dn_{\text{lyst}} + \left(\frac{\partial G}{\partial n_{\text{late}}}\right)dn_{\text{late}} \quad (10)$$

where as $\frac{\partial G}{\partial T} = -S$ and $\frac{\partial G}{\partial P} = V$

$$dG = -SdT + VdP + \mu_{\text{lyst}}dn_{\text{lyst}} + \mu_{\text{late}}dn_{\text{late}} + \mu_{\text{aq}}dn_{\text{aq}} + \mu_{\text{ACN}}dn_{\text{ACN}} \quad (11)$$

The chemical potential (μ) for the photocatalyst and dye are $\mu_{\text{lyst}}dn_{\text{lyst}} = 0$ and $\mu_{\text{late}}dn_{\text{late}} = 0$ respectively during PCR at $dT \geq 0$ and $dP \geq 0$. Therefore, $F = C - P + x_i$, where x_i is an electronic variable attained *via* essential variables (E_v) such as robust holes, synchronization, wavefunctions, and FRET. The critical variables (C_v) at dT and dP are $h\nu$ and FRET, expressed as A_v by eqn (12):

$$F = C - P + [E_v + C_v + A_v] \quad (12)$$

Eqn (12), with C_{QMA} having QMA is expressed as eqn (12a).

$$F = C_{\text{QMA}} - P + [E_v + C_v + A_v] \quad (12a)$$

The $\mu_{\text{late}}dn_{\text{late}} = \mu_{\text{lyst}}dn_{\text{lyst}} = C_{\text{QMA}}$ stable, as C_{QMA} is stoichiometrically constant as $=C_{\text{QMA}} - P + [E_v + C_v + A_v]$. On PCR, the molecularity of the dye remains the same except for the conversion of its Cl^- secondary bond into covalent bond, so Cl^- could not be ascertained as an E_v . $h\nu$ also initiated the $2\text{Cl}^- + 2\text{h}^+ \rightarrow \text{Cl}_2$ secondary chemical process. The 2h^+ are not generated as a fragment of IQ or solvent rather Cl^- has come out of QMA of (h^+) holes. Cl^- neither adding nor subtracting dye alters the stoichiometric input of C_{QMA} in PCR. $2\text{Cl}^- + 2\text{h}^+ \rightarrow \text{Cl}_2$ in the PCR of dye *in situ* balances the holes at quaternary N at constant C_{QMA} to calculate F . The $=C_{\text{QMA}} - P + [E_v + C_v + A_v]$, C_{QMA} relates a dye with photocatalyst, while the e^- and h^+ balance the E_v . $\pi \rightarrow \pi^*$, $n \rightarrow n^*$, and $\sigma \rightarrow \sigma^*$ of the photocatalyst with minimum Prigogine dS streamline the holes acting as E_v . The $F = C_{\text{QMA}} - P + [E_v + C_v + A_v]$ or $=C_{\text{QMA}} - P + x_i$; where



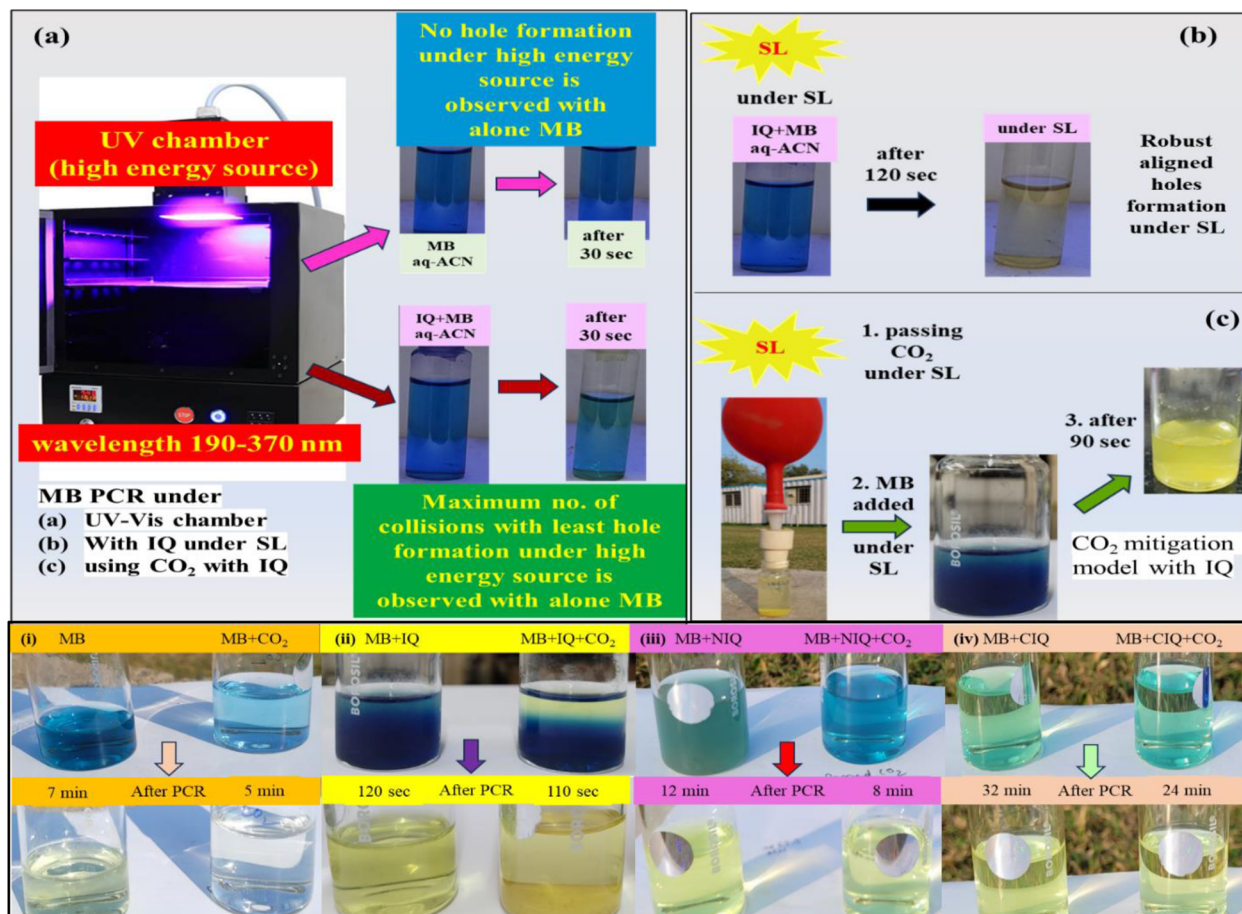


Fig. 13 MB dye PCR at initial and final states under (a) UV-Vis chamber, (b) SL with IQ, (c) CO₂ with IQ and (i) alone MB, MB + CO₂ (ii) MB + IQ, MB + IQ + CO₂ (iii) MB + NIQ, MB + NIQ + CO₂ (iv) MB + CIQ, MB + CIQ + CO₂ under SL.

$x_i = E_V, C_V, A_V$ (constant flow of $h\nu$). The μ of C , at dT and dP for the PCR is $dG = \sum_{i=1}^n n_i d\mu_i$ (Gibbs – Duhem equation) where n moles of photocatalyst are constant with $d\mu_i = 0$ for generating holes without structural changes.^{31–33} The $dG = 0$, $\mu = \left(\frac{dG}{dn_{\text{lyst}}}\right) dn_{\text{lyst}} = 0$ or $\mu = 0$ unlike $\mu = \left(\frac{dG}{dn_{\text{dye}}}\right) dn_{\text{dye}}$ with $\mu \neq 0$, as variables for the PCR, as eqn (13).

$$dG = n_{\text{lyst}} d\mu_{\text{lyst}} + n_{\text{late}} d\mu_{\text{late}} \quad (13)$$

$$dG = \chi = n_{\phi_{\text{lyst}}} d\mu_{\text{CB-VB}} + n_{\phi_{\text{late}}} d\mu_{(\text{holes}_{\text{initial}}) - (\text{holes}_{\text{afterPCR}})}$$

$dG < 0$ infers dye PCR without degrading into $n_1, n_2, n_3, \dots, n_n$ molecules (χ = PCR efficiency). On receiving $h\nu$, water split is one of the prominent factors. $n \rightarrow n^*$ and $\pi \rightarrow \pi^*$ together generate $\psi(x, t)$ as the $2s^2$ electron with N^+ of MO oscillate within $2s^2 \rightarrow 2s^0$ (Fig. 12). N^+ connects an electron-rich π bond at the phenyl ring on the right side, while an ERG on the left side generates wavefunctions with negative charge (ψ_-) connecting ψ_+ as QMA. No electronic charge on N^+ existed that could have bypassed to the π bond on RHS while the ψ_- of ERG stabilizing

ψ_+ of N^+ via FRET. The wavefunction simulating activities normalize somewhere at a margin via an orthogonal mechanism with a differential integral. The $(\psi_{\text{CH}_3} \times \psi_{\text{CH}_3})[\psi_+] \times \psi_{\pi\text{N}=\text{C}}$ conjugated states of $((\text{CH}_3)_2\text{N}=\text{C})$ might have counterbalanced the DOS of N^+ (Fig. 12). The rotational and vibrational motions might have been equipartitioned even with X^- anion like Cl^- , and the N^+ might have been stable. The MO with IQ assisted by solvent split via C_{QMA} reorienting its eigenenergies in one plane and MO with aq-ACN dipoles has optimized a quinonoid state. The same experiments were conducted by mixing CO₂ with IQPs for MB reduction and analysed by UV-Vis (Fig. 13). The IQ, NIQ, and CIQ have photocatalytically reduced MB in 120 s, 12 and 32 min while with CO₂ in ~ 90 s, 8 and 24 min respectively (Fig. 13 and 14). CO₂ with LPE and π bonds on getting realigned with IQ have robustly generated holes reducing MB and QHIn in ~ 90 s and 10 min, acting as a photocatalyst. The CO₂ and IQ mutually align energies as eqn (13a) to photocatalytically reduce MB:

$$k_B T = \frac{h}{2\pi} \sqrt{\frac{k}{\mu}}; \mu_{\text{IQ} \cdot \text{CO}_2} = \frac{m_{\text{IQ}} m_{\text{CO}_2}}{m_{\text{IQ}} + m_{\text{CO}_2}} \quad (13a)$$

The $h\nu$ interacts with the π (sp^2) electrons and LPE of aligned IQPs + CO₂ for VB and CB ROCs respectively and shares their

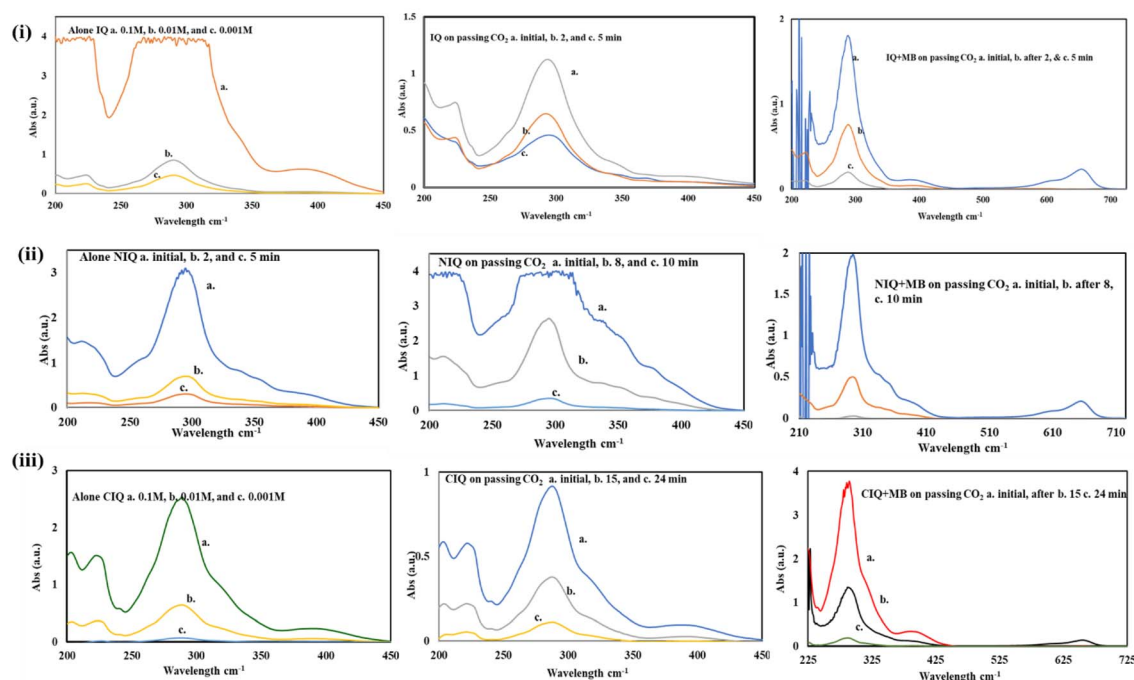


Fig. 14 Initial and final states (i) alone IQ (a) 0.1, (b) 0.01, (c) 0.001 M, IQ + CO₂ & MB + IQ + CO₂ at (a) initial, (b) 2, (c) 5 min (ii) alone NIQ (a) 0.1, (b) 0.01, (c) 0.001 M, NIQ + CO₂ & MB + NIQ + CO₂ at (a) initial, (b) 8, (c) 10 min (iii) alone CIQ (a) 0.1, (b) 0.01, (c) 0.001 M, CIQ + CO₂ & MB + CIQ + CO₂ at (a) initial, (b) 15, (c) 24 min under SL.

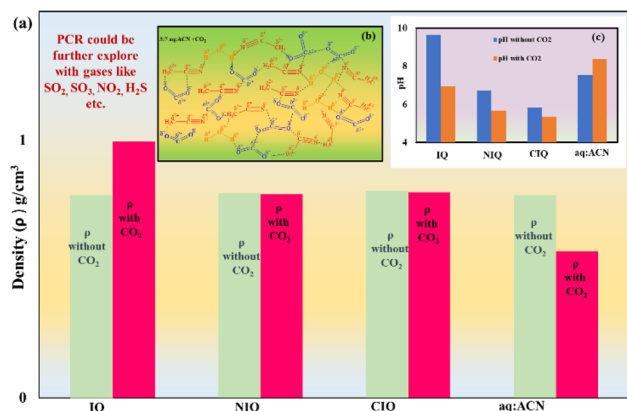


Chart 2 Alone IQPs physicochemical properties (density and pH) w.r.t. with CO₂ favouring dye PCR.

eigenenergies with the π (sp^2) electrons of a dye reducing to leuco state (LMB). CO₂ with polar IQ has acted as a photocatalyst developing strong dipole-dipole interactions mutually and with aq-ACN to photocatalytically reduce a dye with higher catalytic efficiency (~ 90 s) and mitigating CO₂ to carbonic acid with $6n \rightarrow 6n^*$ and $\pi \rightarrow \pi^*$. The IQ, NIQ, and CIQ with 3 : 7 aq-ACN without CO₂ have produced densities (ρ) of 0.784406 (9.64), 0.794179 (6.72), and 0.802968 g cm⁻³ (pH = 5.84) respectively. While IQPs with CO₂ have produced the ρ 0.996047 (6.95), 0.790151 (5.68), and 0.797624 g cm⁻³ (pH = 5.35) respectively (Chart 2). CO₂ has increased the density with IQ as it split the water and activate the CO₂ to form carbonic acid lowering pH

from 9.64 to 6.95 (Fig. 15). The densities of alone water (0.997), ACN (0.786), and 3 : 7 aq-ACN (0.568 g cm⁻³) at 25 °C are also lower than the IQ mixed with CO₂ that have credited to the stronger dipolar-dipolar interactions. This could be helpful for monodispersion and hole generation for the PCR of MB and QHIn in ~ 90 s, 17 min than without CO₂ in ~ 120 s, 24 min respectively (Fig. 16). The sound velocity 1507.01, 1289.83, and 1298.85 m s⁻¹ for IQ, NIQ, and CIQ than 1510.35, 1283.44, and 1291.43 m s⁻¹ with CO₂ respectively supported the dye PCR mechanism.

Plausible mechanism to photocatalytically reduce dyes in the presence of CO₂ with IQPs

Step 1: $SL(h\nu) + IQ + CO_2 \rightarrow IQ^* + CO_2^* \rightarrow \approx nh^+ + ne^-$;

Step 2: $SL + 2H_2O \rightarrow 4H^+ + 2O_2^{2-}$ ($h\nu$ split); $4H^+ + 4e^- \rightarrow 2H_2$;
 $2O_2^{2-} + 4h^+ \rightarrow O_2$

Step 3: $IQ^* + h\nu + CO_2^* + H^+ + dye \rightarrow H_2CO_3 \rightarrow IQ^* + reduced\ dye + H^+ + HCO_3^-$

IQ has acted as a moisture-sensing agent for water splitting to form carbonic acid. The carbonyl of IQ and the carboxylic group of carbonic acid aligned nearby *via* stronger interactions that might have orientated them in the same phase for generating robust ROC. However, NIQ and CIQ have lowered the density due to NO₂ and Cl FG inducing a polarity differently by weakening the intermolecular interactions and forming carbonic acid with pH 5.68 & 5.35 respectively. The molecules like IQ lacking any FGs with symmetrically aligned π conjugated configuration could act as robust photocatalysts for the PCR of a dye than its derivatives differing by the presence of FG.



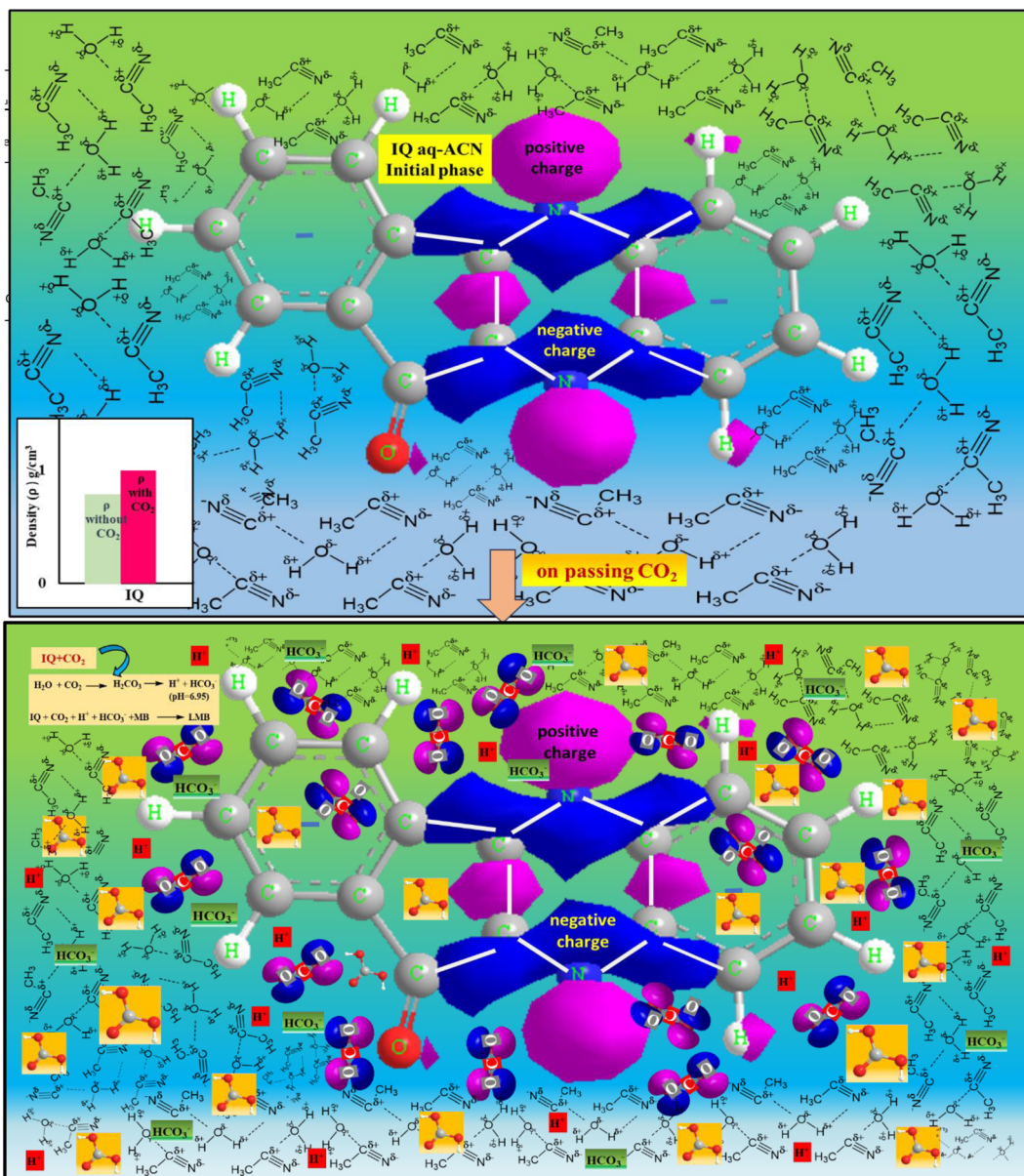
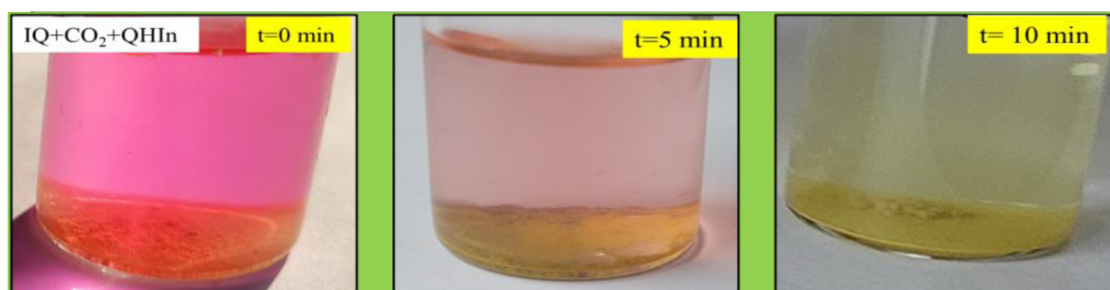
Fig. 15 IQPs with CO₂ MB PCR mechanism.Fig. 16 QHIn PCR using IQ with CO₂ at $t = 0, 5$, and 10 min.

Table 1 PCR of MB (18 ppm) using IQPs and SIQPNO₂ (1.5 ppm) in aq-ACN under SL

Sr. no.	Sample	MB reduction time (~min)		Rate of PCR (%)	
		aq-ACN	Dye abs (%)	aq-ACN	aq-ACN (~g min ⁻¹)
1	IQ	2	86.0	43.0% min ⁻¹	15.0 × 10 ⁻²
2	NIQ	12	80.7	6.7% min ⁻¹	2.5 × 10 ⁻²
3	CIQ	32	71.1	2.2% min ⁻¹	1.0 × 10 ⁻²
4	SIQPNO ₂	190	86.5	0.45% min ⁻¹	0.16 × 10 ⁻²

This is the 1st study of PCR dyes using IQPs with CO₂ to reduce dye with mitigation to carbonic acid formation (Fig. 15 and 16).

UV-vis adsorption activity of IQPs and SIQPNO₂ to photocatalytically reduce dyes

The MB PCR rates were determined using eqn (14) and with IQ, the rate is as follows:

$$r = \frac{d(\text{reduction})}{dt} \text{ or } \frac{86.0\%}{2 \text{ min}}, r = 43\% \text{ min}^{-1} \quad (14)$$

The % MB PCR by IQ in 2 min was calculated using eqn (15):

$$\frac{C_0 - C_t}{C_0} \times 100\% \text{ or } = \frac{0.01874 - 0.00261}{0.01874} \times 100, \text{ or } 86.0\%, \quad (15)$$

where C_0 is the initial % MB concentration at $t = 0$ and C_t is the reduced % MB concentration at time t . NIQ and CIQ were photocatalytically reduced in 12 and 32 min with 80.7 and 71.1% respectively. The % MB PCR by IQ + CO₂ in 90 s was calculated using eqn (16):

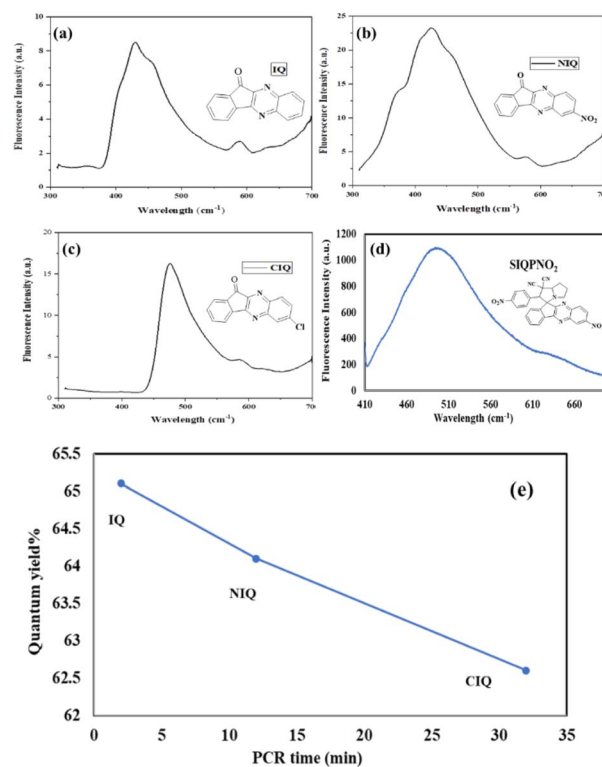
$$\frac{C_0 - C_t}{C_0} \times 100\% \text{ or } = \frac{0.01874 - 0.002001}{0.01874} \times 100, \text{ or } = 89.3\% \quad (16)$$

The reduced % MB concentration by NIQ + CO₂ in 8 min is $\frac{C_0 - C_t}{C_0} \times 100 = \frac{0.01874 - 0.00290}{0.01874} \times 100$, or = 84.5%. The % MB PCR by CIQ + CO₂ in 24 min was calculated using eqn (17):

$$\frac{C_0 - C_t}{C_0} \times 100 \text{ or } = \frac{0.01874 - 0.00495}{0.01874} \times 100, \text{ or } 73.5\% \quad (17)$$

The PCR of MB by IQ (86.0) > NIQ (80.7) > CIQ (71.1) % was calculated using eqn (14)–(16) while with CO₂ using eqn (17) (Table 1). UV-Vis analysis for MB, MO, RhB, and BBR individually by IQPs and SIQPNO₂, and collectively by SIQPs with LGT, infer IQPs as robust photocatalysts (Fig. S9 and S10†). The higher MB PCR with IQ in 2 min compared to 12, 32, and 180 min with NIQ, CIQ, and alone SIQPNO₂ infer IQ as an up-conversion nanophotocatalyst to store a higher energy (Table S6†).

The dyes which have quaternary atoms, π -conjugated systems, LPE, extended double bonds, and fewer peripheral ERGs interfaced with those of the IQPs and SIQPNO₂ via FRET to photocatalytically reduce with higher Φ . The IQ was 5 times reusable to photocatalytically reduce dyes without structural

**Fig. 17** Fluorescence of (a) IQ, (b) NIQ, (c) CIQ, (d) SIQPNO₂, and (e) Φ vs. PCR time graph.

degradation, the IQPs and SIQPNO₂ were reusable to reduce dyes on washing with chilled water and ethanol and dried at 100 °C for 6 h. The 0.001 M MB, MO, BBR, and RhB each was mixed with IQ for PCR, and after washing, IQ was further mixed in 0.001 M each dye. IQ after washing was used up to 5 cycles reducing 99% dyes in 2, 5, 12, 21, and 36 min respectively on

Table 2 UV-Vis & fluorescence study of IQPs and SIQPNO₂ in aq-ACN (1.5 × 10⁻³ M) at λ_{exc} = 295, 285, 295 nm (IQPs) & 285 nm (SIQPNO₂), $\Delta\lambda = (\lambda_{\text{em}} - \lambda_{\text{exc}})$ nm with specific ϵ_{max} (M⁻¹ cm⁻¹)

Molecules	λ_{max}	Abs	ϵ_{max}	λ_{em}	$\Delta\lambda$	I_f	Φ
IQ	292	0.2	199	453	158	8.9	65.1
NIQ	278	0.4	266	444	159	23.6	64.1
CIQ	293	0.6	406	471	176	18.6	62.6
SIQPNO ₂	278	0.8	533	496	285	1085.2	57.4



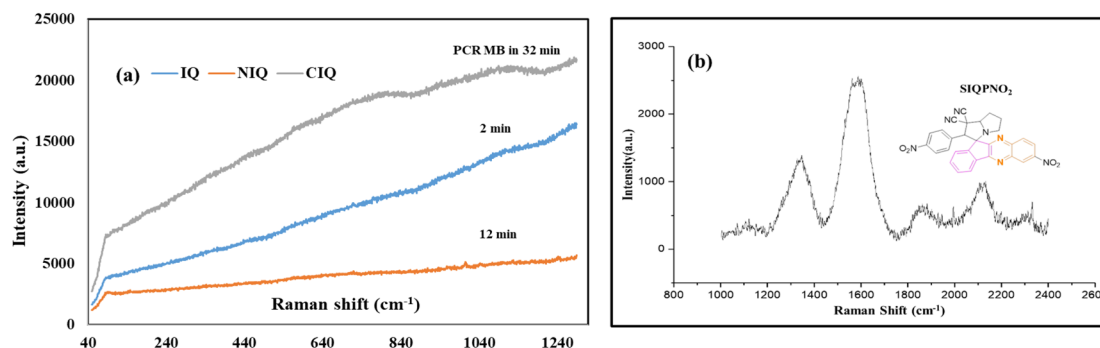


Fig. 18 Raman spectra of (a) IQ, NIQ, CIQ, and (b) SIQPNO₂.

Table 3 Raman slope for IQPs at different Raman shift (S_R) vs. intensity I_R (a.u.) at specific frequency

Sr. no.	S_R (cm ⁻¹)	I_R (CIQ)	I_R (IQ)	I_R (NIQ)
1	91.8142	7236	3830	2662
2	797.248	18 836	10 604	4326
3	1223.86	21 018	15 042	5168

repeating the same procedure for PCR efficiency. After the 5th cycle, almost 10% reduction efficiencies with IQPs and SIQPNO₂ were noticed. PCR efficiencies decreased due to surface occupancy with dyes or nanoclustering. Zhu *et al.*, studied lowering in PCR efficiency of RhB using Zn-Al-Ce-MMO after 6 runs.³⁴ Elsayed *et al.* examined Na-doped ZnO NPs reducing 80% of MB after 7 runs.³⁵ IQPs and SIQPNO₂ photocatalytically reduced in 2–30 min than Zn-Al-Ce-MMO and Na-doped ZnO NPs in 60–74 min.

Fluorescence spectra analysis

Fluorescence emitted wavelengths (λ_{em}) for IQ, NIQ, CIQ, and SIQPNO₂ are 453, 444, 471, and 498 nm at 295, 285, 295, and 285 nm excited wavelength (λ_{exc}) respectively (Fig. 17(a–d) and Table 2). Their fluorescence intensity (I_f), Stokes shift ($\Delta\lambda$), and Φ were calculated as follows:



$$K_{eq} = \frac{[SIQPNO_2^*][h^+][e^-]}{[SIQPNO_2][h\nu]} \quad (18)$$

SIQPNO₂ with milder λ_{em} than IQ infer unsynchronized transitions, detaining maximum eigenenergies (Fig. 17, eqn (17) and (18)). The higher $I_f = 23.6$ (a.u.) for NIQ at 444 nm with shorter λ_{em} synchronizes manifold intramolecular transitions through different DOS, absorbing higher energy, unlike IQ. Lowest I_f and $\Delta\lambda$ values of IQ than NIQ, CIQ, and SIQPNO₂ infer synchronized eigenenergies (Fig. 17). The SIQPNO₂ photocatalytically reduced MB in 190 min due to the weakest FRET with highly disordered intramolecular transitions unable to overcome QEB. SIQPNO₂ having two NO₂ EWG at terminal positions drastically aligns electronic densities that hurdled the

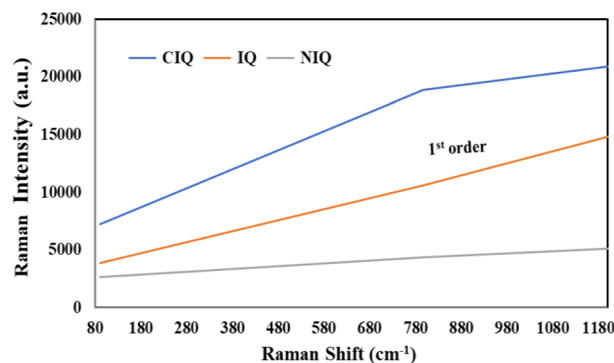


Fig. 19 Raman shift (S_R) vs. intensity (S_R) for IQPs.

hole generation and could not photocatalytically reduce QHIN even after 48 h; however, the studies are continued. NO₂ at phenyl of SIQPNO₂ connected to pyz with maximum transitions in different energy-storing domains instead of emittance had enhanced the PCR time. The CIQ streamlines an electron flow, generating the electron-deficient sites, unlike NIQ. The I_f value of EWG and ERG activities has correlated the PCR time with reference to a least I_f 8.9 (a.u.) with IQ than NIQ, CIQ, and SIQPNO₂ having 23.6, 18.6, and 1085.2 (a.u.) respectively (Fig. 17). Both NIQ and CIQ have intensified energy holding capacities with a shorter PCR time. The $I_f = 1085.2$ (a.u.) for SIQPNO₂ PCR in 190 min unlike 167 (a.u.) for SIQPI in 95 min in 1:6 and 1:2 ratio of time respectively infers intramolecular electronic transitions (Fig. S11†).¹⁸ NO₂ of SIQPNO₂ inhibits a PCR rate, unlike IQ exhibits the least I_f and shortest PCR time (Table 2). The Φ value for IQ, NIQ, CIQ, and SIQPNO₂ calculated at λ_{exc} 295, 285, 295 & 285 nm has determined $E = 6.734 \times 10^{-19}$ J (IQ & CIQ) and 6.970×10^{-19} J (NIQ & SIQPNO₂) respectively. The number of $h\nu$ absorbed (n_a) was calculated using eqn (19) as follows:

$$IQ(n_a) = \frac{6.734 \times 10^{-19} \text{ J}}{6.626 \times 10^{-34} \text{ J s}}; \text{ or } IQ(n_a) = 1.016 \times 10^{15} \text{ s}^{-1} \quad (19)$$

The n_a values for NIQ, CIQ, and SIQPNO₂ are 1.052×10^{15} , 1.016×10^{15} , and $1.052 \times 10^{15} \text{ s}^{-1}$ at λ_{em} of IQ, NIQ, CIQ, and SIQPNO₂ at 453, 444, 471, and 496 nm with $E = 4.385 \times 10^{-19}$,



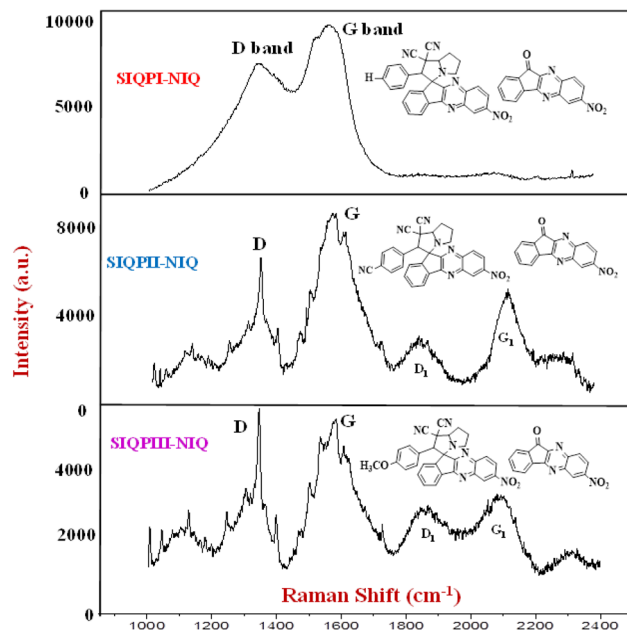


Fig. 20 Raman spectra for SIQPI + NIQ, SIQPPII + NIQ, and SIQPPIII + NIQ.

4.474×10^{-19} , 4.217×10^{-19} , and 4.005×10^{-19} J respectively (Table 2). The number of $h\nu$ s emitted (n_e) by IQ is calculated using eqn (20):

$$IQ(n_e) = \frac{4.385 \times 10^{-19} \text{ J}}{6.626 \times 10^{-34} \text{ J s}} \quad (20)$$

The n_e values for NIQ, CIQ, and SIQPNO₂ are $0.662 \times 10^{15} \text{ s}^{-1}$, 0.675×10^{15} , 0.636×10^{15} , and $0.604 \times 10^{15} \text{ s}^{-1}$. The Φ , ratio of n_e and n_a was obtained with IQ using eqn (21):

$$\Phi_{IQ} = \frac{n_e}{n_a} \times 100\% = \frac{0.662 \times 10^{15} \text{ s}^{-1}}{1.016 \times 10^{15} \text{ s}^{-1}} = 65.1\% \quad (21)$$

The Φ value for NIQ, CIQ, and SIQPNO₂ are 64.1, 62.6, and 57.4% respectively, while 65.1% with IQ seem to minimize EER (Fig. 17 and Table 2). IQPs with negligible I_f than SIQPNO₂ infer disordered $\pi \rightarrow \pi^*$ and $n \rightarrow n^*$. Aq-ACN affects λ_{max} and ϵ_{max} as bathochromic $\pi \rightarrow \pi^*$ and hypsochromic shifts $n \rightarrow n^*$ of FG.³⁶ IQPs and SIQPNO₂ both with bathochromic shifts ($\Delta\lambda =$

λ_{285} and $\lambda_{295} < \lambda_{\text{em}}$), at shorter λ_{em} , and I_f have widened applications *vis-à-vis* Φ , λ_{em} , and I_f for the PCR of a dye (Table 2 and Fig. 17). PCR studies using IQPs, IQPs + LGT, SIQPNO₂, SIQPNO₂ + LGT, SIQPNO₂ + NIQ, and SIQPs + NIQ have reduced MB, MO, BBR, and RhB and were studied with fluorescence (Fig. S11–S24†).

Raman analysis

IQPs and SIQPs photosensitive molecules reengineer the overall eigenenergies to electronically align with single-valued wavefunctions, expressed as a deformed DOS. The Raman intensity (I_R) elucidates the optimized molecular oscillations differentiating the ERG and EWG activities expressed as multiple D and G bands despite synergistic structure minimized I_R on stabilizing dipoles (Fig. 18 and eqn (22)).

$$\text{Energy}(E) = h\nu, \quad = \frac{hc}{\lambda}, \quad \tilde{\nu} = \frac{1}{\lambda}, \quad E = hc\tilde{\nu} \quad (22)$$

The 1st order of Raman shift (S_R) vs. I_R with IQ inferred transition energy states generating dipoles at a similar rate. The $\Delta G = \Delta H - T\Delta S$ with $\Delta G = 0$ infers oscillated dipoles with a laser within similar dimensions on regaining ΔH . Else any bonded atom pair would have been opted out of stabilization with different eigenenergy (E_ψ) as in eqn (23):

$$E\psi = \frac{\partial^2}{\partial x^2} \psi + v(x, t)\psi_i \quad (23)$$

The I_R vs. S_R in 1st order infers uniform PE exchanging into $\frac{\partial^2}{\partial x^2}$ KE via symmetric $\psi_i(x, t)$ oscillations at distance x in time t as per Heisenberg.^{37–39} The absence of D & G bands infers $\Delta G = \Delta H - T\Delta S$, at $\Delta G = 0$, $\Delta H = T\Delta S$, or $\Delta S = \frac{\Delta H}{T}$ and $E(\psi) = \left(\frac{p^2}{2m}\psi(x, t)\right)\psi$ via $\frac{\partial}{\partial t}\left(\frac{p^2}{2m}\right) = -\frac{\partial}{\partial t}(v(x, t))$. The $\frac{\partial}{\partial t}\left(\frac{p^2}{2m}\right) \approx T\Delta S$ could twist a bond with ΔH on oscillation. The IQ as a harmonic oscillator minimized undesired collisions reducing MB in ~ 2 min with uniform S_R . The partially equilibrated two centers of NIQ respond differently to $h\nu$ rather than generating holes to photocatalytically reduce dyes. EWG influences an electron cloud without deformation, and on passing a laser to IQPs, few electrons are easily excited while forbidding the other transitions due to an integrated framework. On

Table 4 Raman D & G with E_a levels for IQPs, SIQPs with NIQ, and SIQPNO₂

Compounds	E_1 (J) $\times 10^{-31}$	E_2 (J) $\times 10^{-31}$	E_3 (J) $\times 10^{-30}$	E_4 (J) $\times 10^{-30}$	E_5 (J) $\times 10^{-30}$
IQ	1st order (no T.S)				
NIQ	1st order				
CIQ	5.2	7.29	—	—	—
SIQPI + NIQ	8.55	1.06	1.57	—	—
SIQPPII + NIQ	8.88	1.06	1.24	1.42	—
SIQPPIII + NIQ	8.84	1.05	1.22	1.40	—
SIQPNO ₂	8.78	1.06	1.25	1.39	1.54



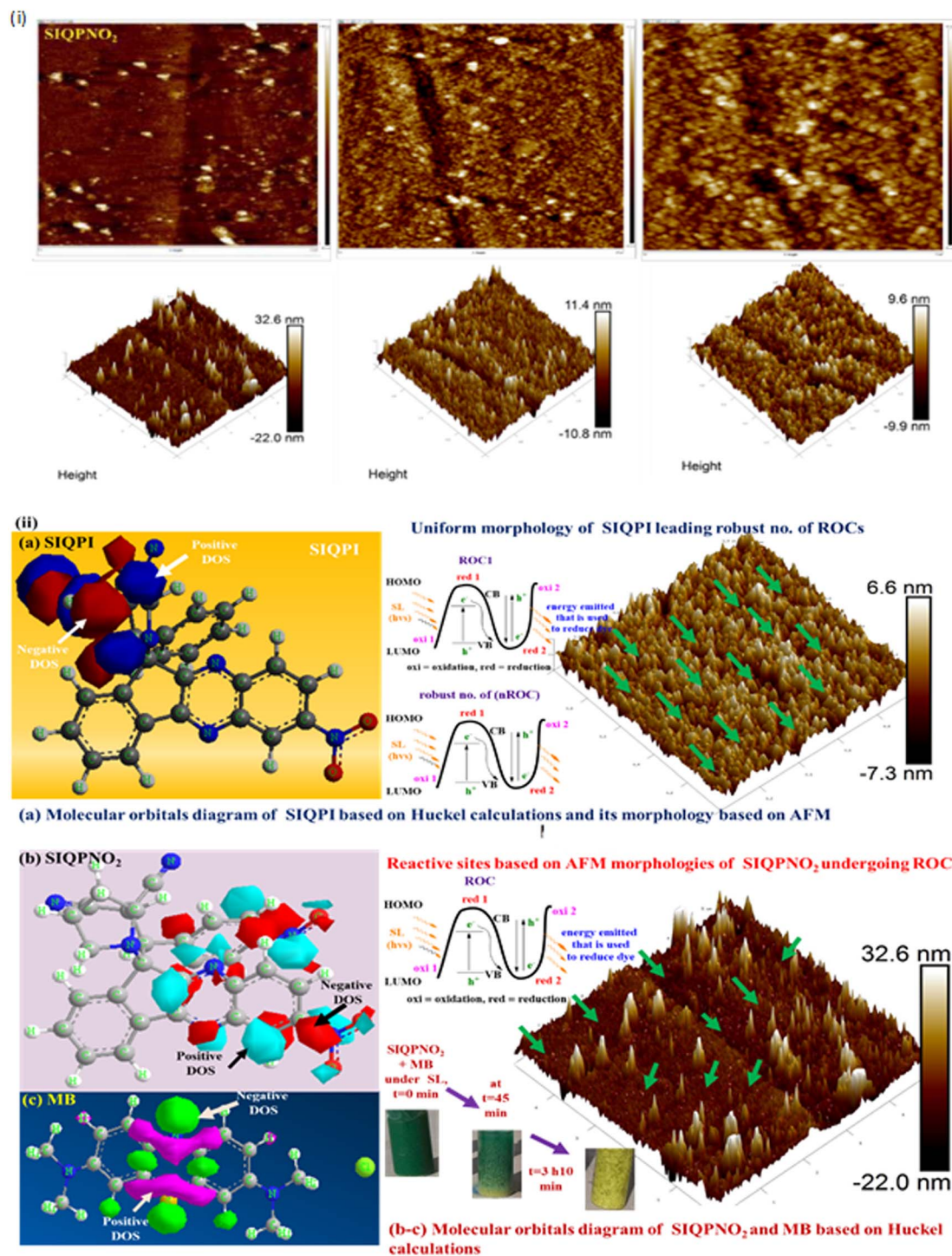


Fig. 21 (i) AFM topography and z axis images of SIQPN0₂ at different dimensions. (ii) Morphology of SIQPI.

acquiring a laser, a new energy-storing alignment within IQPs acts as stocks for reducing the dyes in a shorter PCR time. Moreover, a laser with SIQPN0₂ develops holes, detaining energy as antistokes photocatalytically reduce MB in 190 min. The CIQ generates the weaker antistokes among IQPs due to energy equipartitioning with weaker electronic activities. The SIQPN0₂ with larger Fermi sphere could not crossover QEB as electrons remain in the VB, unlike alone IQPs. SIQPN0₂ has

increased the VB-to-CB volume, elongating the PCR time as the electrons are unable to generate atomic oscillations, unlike NIQ or CIQ, which show vibrant antistokes. The CIQ, IQ, and NIQ are vibrant, moderate, and weakest antistokes with minimum shifts respectively (Table 3). With IQ, the S_R increases linearly along I_R , its higher values reach almost all the electrons to exponentially oscillate in single phase. On lowering an energy of a source, the Raman active stabilized dipoles reduced a dye. Almost all

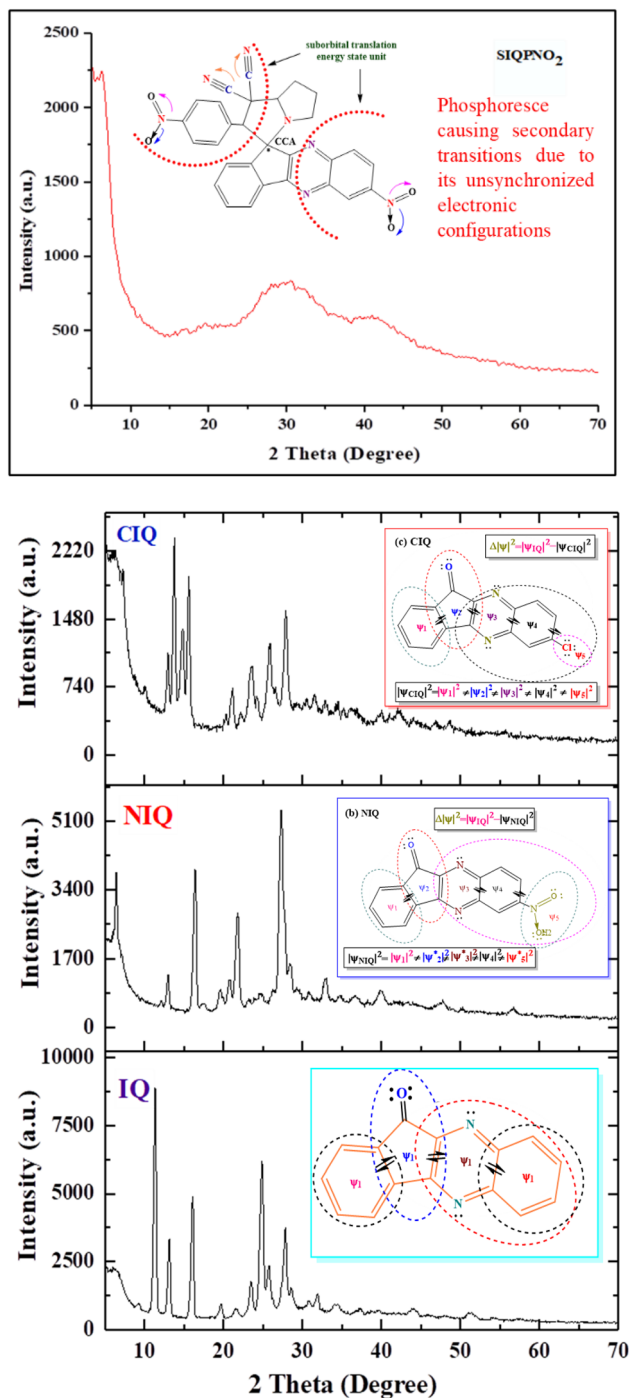


Fig. 22 XRD spectra of SIQPNNO₂ and IQPs.

uniform structures with single and double bonds including N with equal charge develop holes at the same rate. The IQ uniformly oscillates the terminal rings ($\psi_1 = \psi_1 = \psi_1 = \psi_1 = \psi_1$) with a linear slope for MB PCR. NIQ with NO₂ on passing $h\nu$ s reduces MB in 12 min. However, CIQ with a weaker ERG Cl photocatalytically reduced MB in 32 min due to non-equilibrate electronic states by engaging $h\nu$ in different I_R (Fig. 18 and 19).

The CIQ with intramolecular activities mildly generate the holes for PCR in a longer time unlike IQ to crossover QEB PCR dye in 2 min. SIQPNNO₂ with vectorized DOS throughout its functional domains *via* CCA photocatalytically reduce a dye in 180 min as its NIQ delocalized π ring with intensive DOS acting as the 1st oscillating center *vis-à-vis* differently bonded NO₂ FG. The electron–electron cloud reorientations *via* NO₂ attached with FP and CN with pyz ring generating the different DOS. The $h\nu$ could have been received initially by the units developing uniform electronic shifts as no excess photonic energy is left out to reduce dye. NIQ with SIQPI generating intrinsic oscillations analyzed with Raman spectra infers no deformation as D and G bands are absent with non-uniform FRET. Single FRET with IQ infers Raman inactive while with NIQ attains an unequal distribution with a linear curve deforming a shift. The NIQ with SIQPI has synchronized its three domains with many secondary linkages (Fig. 20) without producing a single deformability pattern.

As its individual FG has developed a specific peak for reducing MB in 63 min, unlike 95 min with SIQPI alone. NIQ with EWG oscillates without deformation missing D and G bands. SIQPI having FP, pyz, and NIQ units mixed with NIQ in 1/1 ratio generated the charged centers on lowering a permittivity shortening the PCR time to 63 min unlike 95 min with SIQPI alone. The D and G bands at 1300 and 1700 cm⁻¹ infer mild deformed SIQPI and NIQ as Rayleigh scattering⁴⁰ producing a linear line with mild rate as Raman inactive (Fig. 20). The uniform activity as antistokes scattering avoided undesired collisions during the PCR. The impulse of electrons from one domain to another than of NIQ, pyz, and FP have been prevented by CCA due to trifurcation. Less broad D band than G dominated with Raman active NIQ matrix shortened the PCR time than SIQPI + NIQ on equipartitioning as $G > D$ bands (Fig. 20) with eigenenergies $E\psi$. Aq-ACN SIQPI has reduced 18 ppm MB in 95 min, rate 0.18 ppm min⁻¹ unlike 63 min, rate 0.28 ppm min⁻¹ with SIQPI + NIQ due to a single phase. The NIQ avoids the EEC by equilibrating the oscillations of FP and pyz in continuity *via* CCA. SIQPI alone has produced the least scintillations as a linear line with zero slope without eigenenergies (Fig. 20). Wt loss of alone SIQPI at 110.55 °C (Fig. S25†)¹⁸ unlike SIQPI + NIQ at higher temperature 280–290 °C generating the sharper multiple peaks and has shortened a PCR time.

The NIQ in a same plane as SIQPI having excess LPE and π conjugation with prominent resonating energy $|\psi|^2$ have shortened the PCR time. SIQPI + NIQ with D and G bands infer aligned dipoles at a shorter distance than bandgap with electronically deformed surfaces and bands. The aligned charges synchronized as Gerade symmetry or G band (Fig. 20). Broader D and G bands of SIQPII + NIQ took a shorter PCR time. The laser might have excited the electrons of EWG CN expressed as multifurcated D & G bands with the same energy of SIQPII with NIQ (Fig. 20). However, their DOS interacts differently with CN, pyz electron clouds of phenyl *via* CCA, and NIQ with laser generating multiple holes of wavefunctions (ψ_i). These resonate with the different energies as wavefunctions in the same phase as $I_R = a^2$, where a is the amplitude, and I_R is the resultant

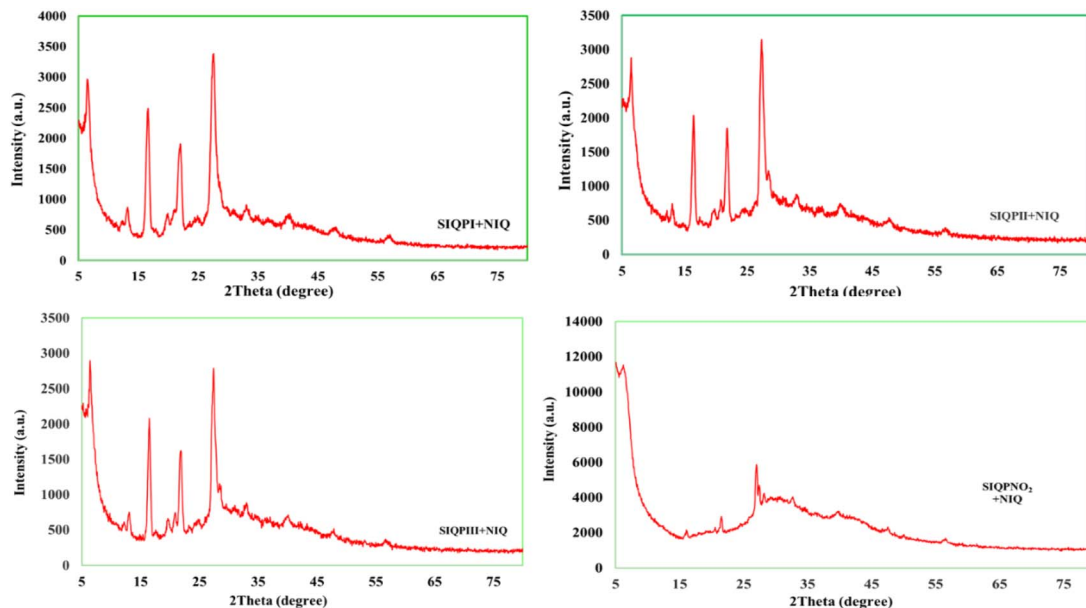


Fig. 23 XRD spectra of SIQPI + NIQ, SIQPPII + NIQ, SIQPPIII + NIQ, and SIQPNO₂ + NIQ.

phonon frequency.⁴¹ The multifurcated peaks broadened at Raman shift 1300 cm⁻¹, 600 a.u. and 1500 cm⁻¹, 5000 a.u. along with 1600 cm⁻¹ small bands (Fig. 20). The 1000–1300 cm⁻¹ aligns with a vibrating Raman shift of the residual domain of SIQPPII + NIQ. The sharper D band infers CN of FP and π bonds of CN of pyz developing a broader frequency, unlike SIQPPII¹⁸ that might have not fully shared their electron to overcome manifold QEB. Resonating energy overcomes QEB in closely placed scintillating intensities expressed as fringes. The bands at 1900 cm⁻¹ at 2100 and 2100 cm⁻¹ at 4100 a.u. infer C=O and NO₂ without mutually resonating energies separately (Fig. 20). The 2N of NIQ along delocalization could have generated the 2nd set of deformation for D and G bands. Raman inactive SIQPI¹⁸ as a weak semiconductor could not align holes but with NIQ disrupted the electronic configuration (Fig. S26(a)†).¹⁸ The DOS of SIQPI + NIQ is more active than synchronized SIQPI alone. The laser could not affect SIQPI unlike splitting into D and G bands with NIQ at 1348 cm⁻¹ with 6000 a.u. and 1581 cm⁻¹ with 10 000 a.u. intermixing (Fig. 20). The bands are broadened by NO₂ at NIQ and NO₂ at FP on symmetric DOS as a new state of oscillations. The NO₂ of NIQ has partially attracted the electron clouds of NO₂ of FP and pyz. The electron-withdrawing activities of NO₂ of FP and NO₂ of NIQ sharpened the bands at 1550 and 1650 cm⁻¹ (Fig. 20). The sharper G band infers a bonding of NO₂ at FP as SIQPI is missing NO₂ at FP as Raman inactive and IR active (Fig. S26(a)†). The 2NO₂ of SIQPNO₂ as Raman active and FT-IR inactive broadened a band at 1900 cm⁻¹ and sharpened at 2000 bifurcating at 2100 cm⁻¹ of NIQ and pyz across CCA. The NIQ with SIQPNO₂ might have sharpened I_R . SIQPPIII alone¹⁸ unlike with SIQPPIII + NIQ produces a straight line by mutually inducing the sharper oscillations lowering QEB. Raman spectra have a sharper split at \sim 1300 cm⁻¹ with a lower intensity due to terminal NO₂ of NIQ. The OME of SIQPPIII could develop coulombic interactions

with NO₂ of NIQ on sharper Raman splits with high intensity compensating the stretching and sharp oscillations. Moreover, various electron-rich and deficient sites have weakened the G band while sharpened the D band for the PCR of MB in 47 min unlike 54 min with SIQPPIII alone (Fig. 20, S26(a)† and Table 4).

AFM analysis

IQP and SIQP photosensitive molecules realign their eigenenergies that dimensionalize a topography expressed as surface-quantized oscillations. This responds to a sharp silicon cantilever tip to scan the interatomic repulsive forces to elucidate the surface activities to receive $h\nu$ accordingly. The surface profiles of SIQPNO₂ did not strongly interact with dye due to its weakly equilibrated electronic clouds and took 190 min to reduce MB (Fig. 21). However, SIQPPII with NIQ has further reduced to 35 min than 63, 47, and 64 with SIQPI + NIQ, SIQPPIII + NIQ, and SIQPNO₂ + NIQ respectively. The SIQPPIII^{3,18} with OMe induces EER with the double bond of the phenyl ring exhibiting a nonlinear topography *via* LPE conjugation, unlike a wavefunction of synchronized topography to capture a maximum $h\nu$ with the intensified surface energies. The wavefunctions of H₃C– (3 σ bonds) with –O– in the conjugated ring intensify the DOS of –OCH₃ and the phenyl ring in response to the EWG exposing the CCA to different eigenenergies of SIQPPIII. The position and nature of FG reorient the surfaces to respond the $h\nu$ as the NO₂ at FP w.r.t. NIQ in opposite directions have confined their respective terminals (Fig. 21(i)). Such re-orientation of eigenenergies generates charge-deficient spaces nearby CCA that intensify eigenfunctions around each NO₂ triggering *in situ* coulombic interactions partially supported with low I_R (Fig. 21). This weakly captures the $h\nu$ and generates the holes and SIQPNO₂ could not overcome QEB and smoothen a topography, resulting in MB PCR in 190 min (Fig. 21(i)). Raman and FT-IR both have confirmed synchronized surface



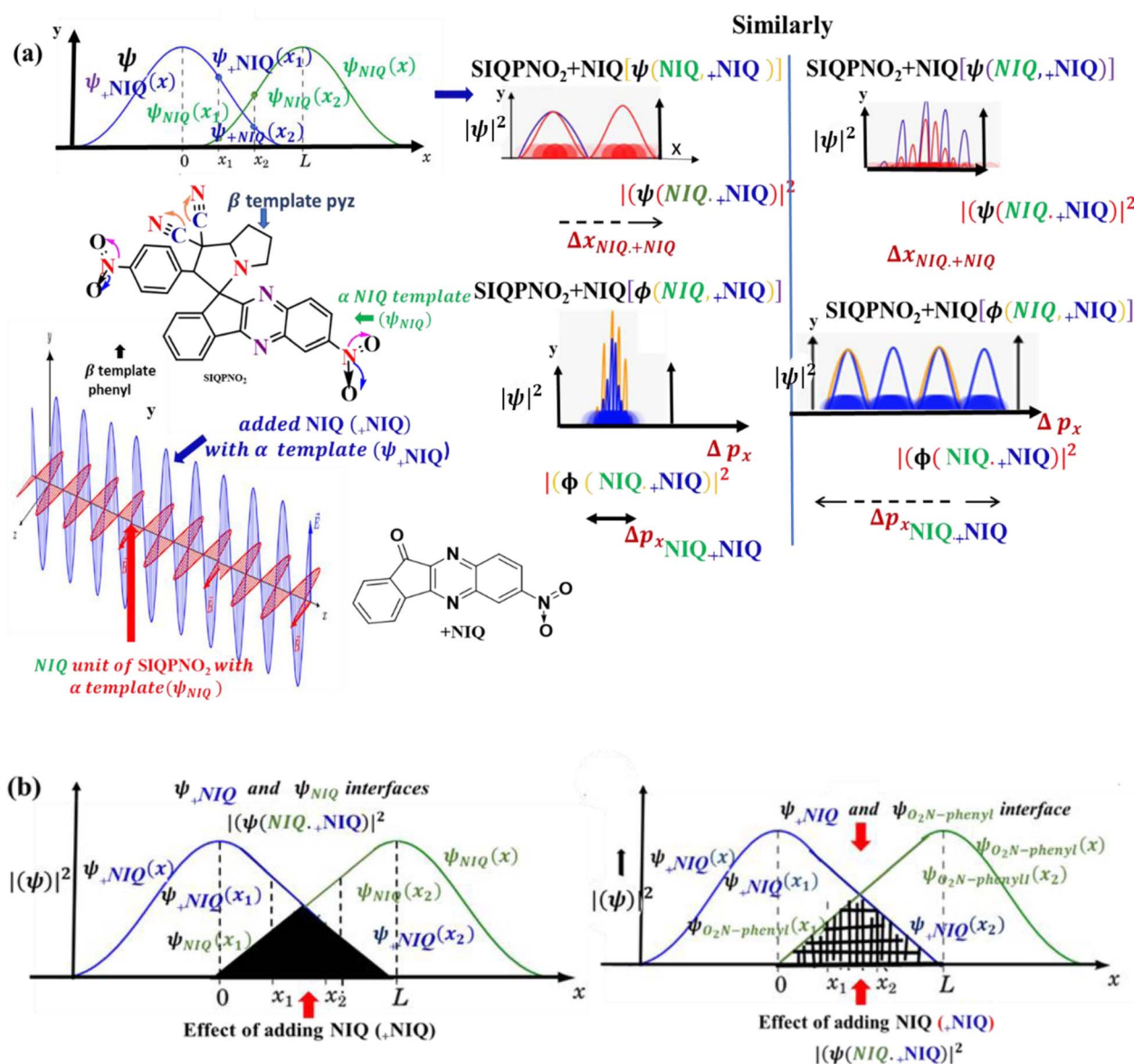


Fig. 24 Dye reducing mechanism of (a) SIQPNQ₂ and (b) role of added (+NIQ) unit on NIQ of SIQPNQ₂ in dye PCR.

residual charges. Surface topography directly influences the efficiency of $h\nu$ absorption, generation of holes, FRET, and reaction kinetics. The less pronounced surface fringes or peripheries, ranging from -22.0 to 32.6 nm, -10.8 to 11.4 nm, and -9.9 to 9.6 nm, infer a lower efficiency in ROC generation and delayed MB PCR to 190 min (Fig. 21(ii)). The larger peripheries provide active reaction sites for the photocatalyst and photocatalate for PCR. SIQPNQ₂ at nanometre scale, such

as nanoparticles or nanosheets, inherently have small surface areas per unit volume, limiting the availability of photocatalate to reach in a vicinity of photocatalyst or to ROC. Meanwhile, the generation of holes and their utilization in reduction get affected as an ordered morphology to facilitate hole generation and alignment to photocatalytically reduce dye and *vice versa*. However, SIQPNQ₂ with a less ordered topography does not facilitate robust hole generation and alignment to reduce a dye,

Table 5 Comparative PCR study of MB, MO, BBR, and RhB using IQPs and SIQPNQ₂

Compounds	MB (PCR min)	MO (PCR min)	BBR (PCR min)	RhB (PCR min)
IQ	2	5	7	12
NIQ	12	18	14	19
CIQ	32	27	28	38
SIQPNQ ₂	190	195	78	392



Table 6 Comparative MB PCR (min) study of alone SIQPNO₂, SIQPNO₂+NIQ, SIQPI + NIQ, SIQPII + NIQ, and SIQPIII + NIQ

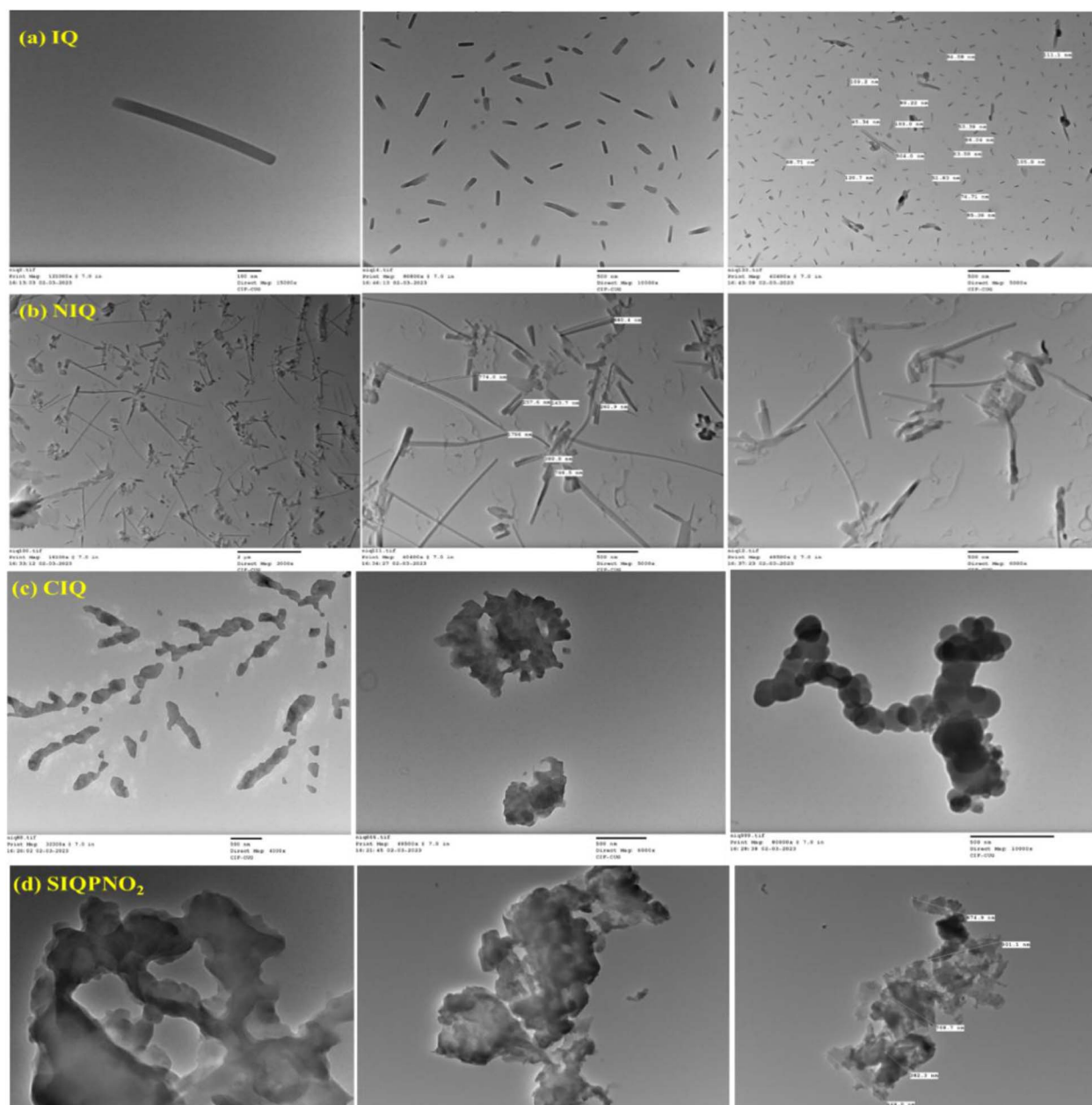
	SIQPNO ₂	SIQPNO ₂ + NIQ	SIQPI + NIQ	SIQPII + NIQ	SIQPIII + NIQ
PCR (min)	190	64	63	35	47

unlike IQPs. SIQPNO₂ with the bulky molecular configuration (pyz, NIQ, & -C₆H₅NO₂) has delayed PCR compared to single-configured IQPs. The two NO₂ and two CN EWG with SIQPNO₂ desynchronize alignment or charge distribution weakens the PCR activity. The less pronounced surface morphology of SIQPNO₂ does not facilitate efficient SL absorption, robust ROC generation, or high quantum efficiency for PCR activities, and

requires more PCR time than IQPs. These IQPs could further be enhanced by functionalizing them with N(CH₃)₂, NH₂, CONH₂, and COOH groups, enabling them to effectively trap renewable energy for dye PCR in a shorter time (Scheme S9†).¹⁸

XRD of IQPs and SIQPNO₂ analysis

XRD analysis determined the lattice plane of the crystal by measuring the atomic placement in terms of peak intensities and *d*-spacing for both IQPs and SIQPNO₂ (Fig. 22). Each integrated constitutional unit, despite having covalent bonds within the IQ framework, has developed sharper peaks in the lattice plane. EWG of NIQ and ERG of CIQ realign Bravais lattice planes of different peaks unlike IQ without FG having sharper peaks (Fig. 22). IQ has produced symmetric charge distribution

**Fig. 25** HR-TEM images of (a) IQ, (b) NIQ, (c) CIQ, and (d) SIQPNO₂.

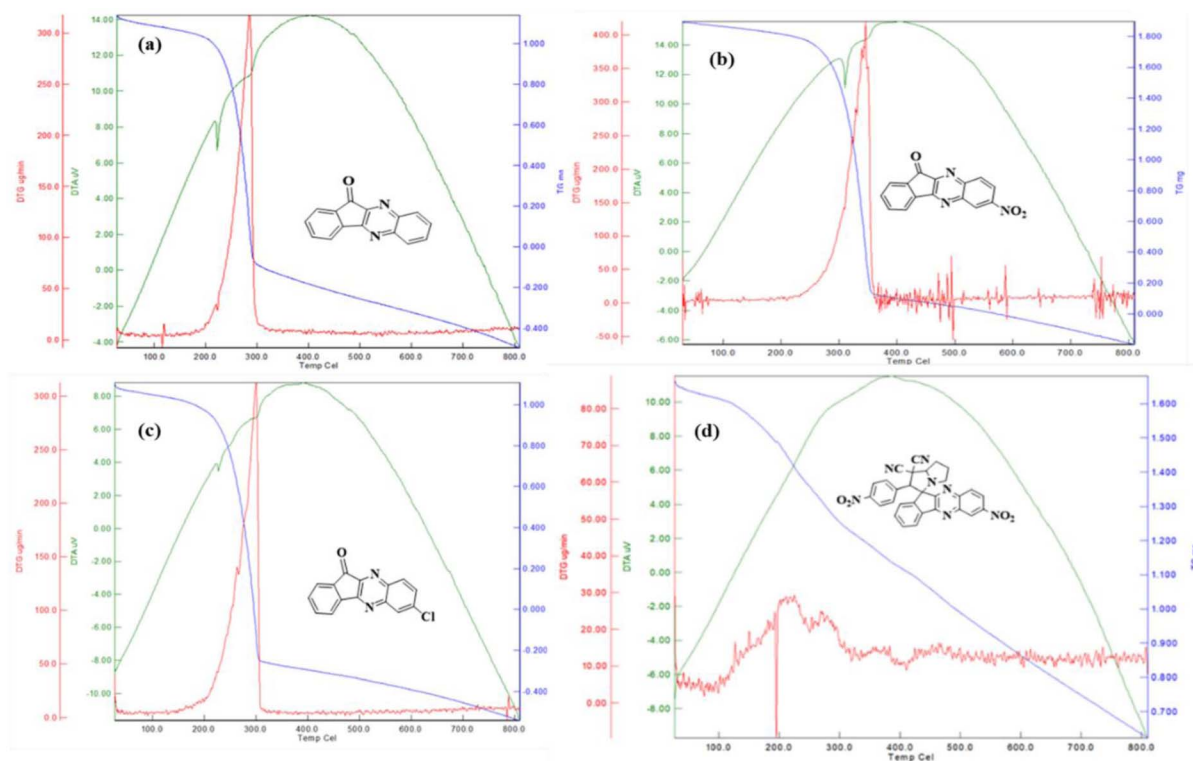


Fig. 26 TGA of (a) IQ, (b) NIQ, (c) CIQ, and (d) SIQPNO₂.

via extended conjugation with electron-rich and -deficient sites. No sharp peak was generated at $2\theta < 10^\circ$ except a sharper lattice at $2\theta \sim 11^\circ$ due to the symmetric plane and bifurcated further by two planes in a single framework (Fig. 22). IQ with oscillations in one plane receives $h\nu$ s without EEC unlike IQ with a maximum of d spacing as its NO₂ withdraws e^- from the delocalized ring influencing structural lattice. Therefore, NIQ with localized and integrated planes has generated lattices at lower $2\theta \sim 5^\circ$. Though the Cl of CIQ could have not overcome its electronic resistance resulting in a loose electronic bridging at $10^\circ < 2\theta < 45^\circ$. That could have aligned CIQ to a nanocrystalline, unlike crystalline IQ and NIQ. The EWG and ERG with NIQ and CIQ have generated sharper lattices at $2\theta \sim 5\text{--}10^\circ$ unlike IQ. The other planes of NIQ and CIQ having π rings are not much affected as their internuclear radii (r nm) between negative (q_1^-) and positive (q_1^+) charges ($q_1^+q_2^-/4\pi\epsilon r^2$) at slightly higher r , nm generate the similar planes at $2\theta = 10\text{--}30^\circ$. The terminal rings of IQPs lie in one plane with sharper intensities. The FG NO₂ and Cl⁻ have disrupted electronic clouds producing their individual lattices. The CIQ increases DOS towards ring-enriching wavefunctions ψ_1 and ψ_3 with ψ_2 having a π system with closely packed lattices (Fig. 22). The wavefunctions ψ_2 infer multiple lattices with CIQ. However, SIQPNO₂ with defused electronic cloud and least split in plane did not respond to $h\nu$ s. SIQPNO₂ acted as a phosphorescent material by generating the secondary transitions due to unsynchronized electronic configurations. SIQPNO₂ with major and minor broad diffraction XRD peaks for two NO₂ at $2\theta \sim 31^\circ$ and 41° due to an amorphous framework

unlike IQPs (Fig. 22). High-intensity peaks at $2\theta \sim 5^\circ$ infer nanostructure with SIQPNO₂.

$$D = \frac{k\lambda}{\beta \cos \theta}; N = \frac{d}{D^3}; \text{ and } \delta = \frac{1}{D^2} \quad (24)$$

D (particle size), with k = constant (0.9), λ = 0.154 nm, 2θ = angle, β = full width of half maximum of a peak^{42,43} (eqn (24)). SIQPNO₂ at $2\theta \sim 8^\circ$ has larger d spacing and 2θ from $\sim 10\text{--}70^\circ$ with a linear curve. Its 2NO₂ at $2\theta \sim 27\text{--}32^\circ$ generated a broader intensity on diffusing its electronic planes responding haphazardly to a laser (Fig. 22). All the planes respond to laser haphazardly without intensifying XRD peaks. NO₂, pyz, and NIQ seem to integrate SIQPNO₂ PE in a single plane indistinguishable towards 2θ . The unique states of PE seem to be integrated by CCA of SIQPNO₂ that generated exceptional I_f . This energy-storing mechanism of SIQPNO₂ could advance the science and technology of organic optoelectronic devices.

Effect of NIQ on SIQPs based on XRD and elemental analysis

NIQ as a photocatalyst has tuned a Fermi energy gap⁴⁴ of SIQPs by generating sharper peaks (Fig. 23). The CCA prohibits the eigenenergies of FP, pyz, and NIQ from mutually mixing, thus, a photocatalyst distinctly sharpens the respective electronic planes. NIQ intensifies the DOS of SIQPI with higher scintillations, resembling a single crystal (Fig. 23). NIQ synchronized the charges of SIQPs to sharpen the planes via FRET shortening the PCR time. The new eigenenergies receive more $h\nu$ for generating the holes with least E_a as the 1st-order reaction (Fig. 23, 24 and Table 5).^{3,45} The scintillation counts of



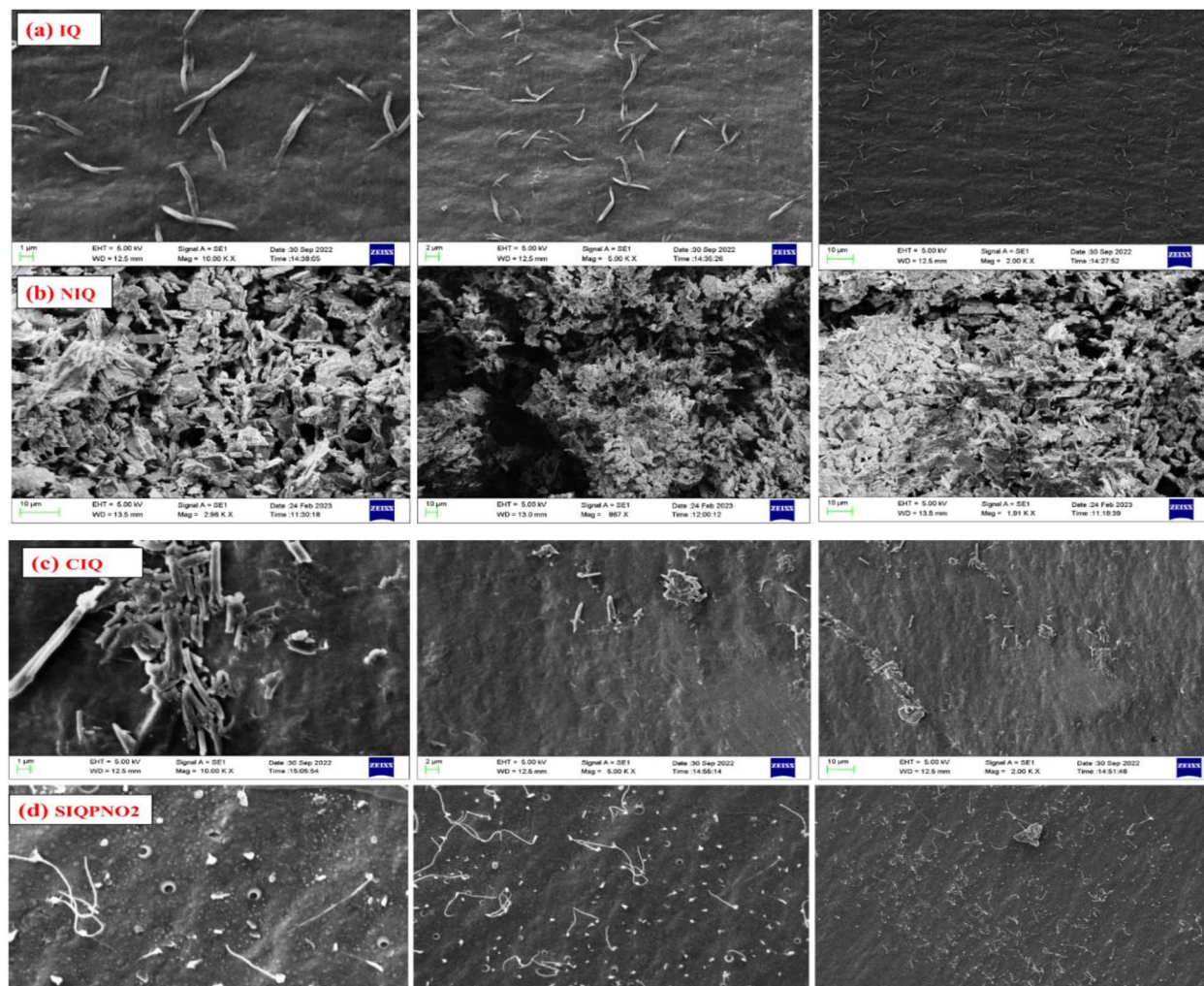


Fig. 27 SEM images of (a) IQ, (b) NIQ, (d) CIQ, and (c) SIQPN0₂.

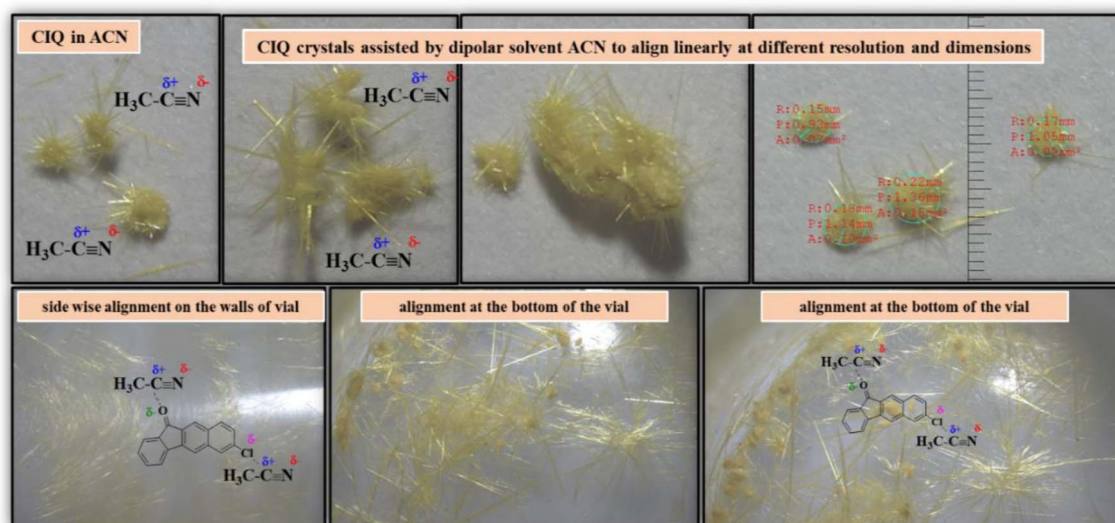


Fig. 28 Stereomicroscopic images of CIQ at different resolutions and dimension in ACN.

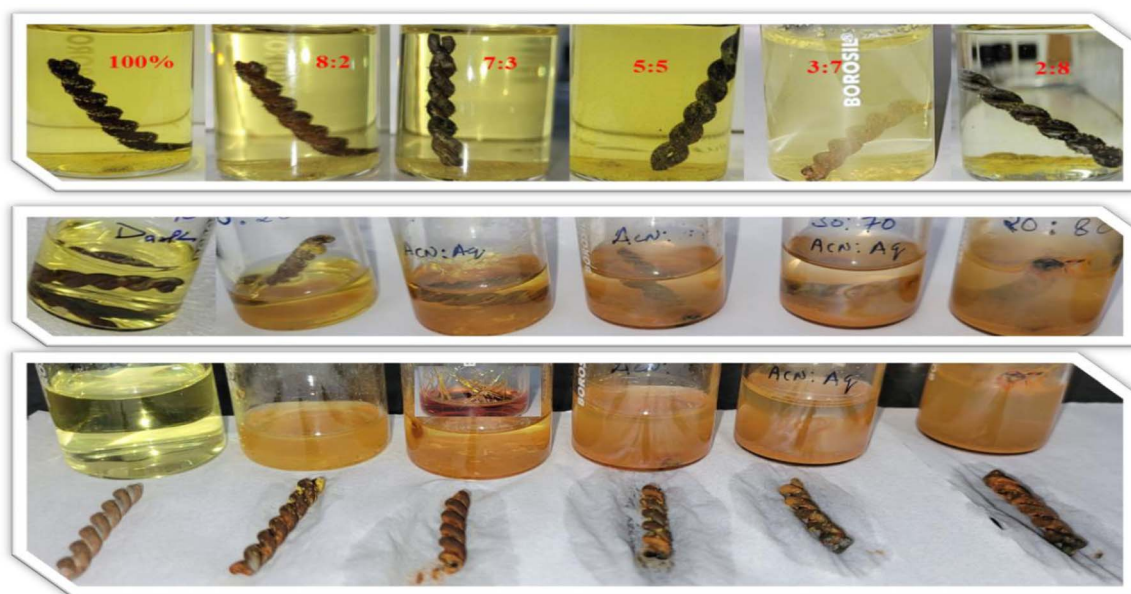


Fig. 29 IQ + Fe in 100% ACN, 8 : 2, 7 : 3, 5 : 5, 3 : 7, and 2 : 8 of aq : ACN initial, after 5 days, and after a week.

SIQPs are counterbalanced with NIQ optimizing their overall structural sites (Fig. 23 and 24) with an integrated structure. However, SIQPNO₂ alone could not sharpen an XRD pattern unlike SIQPNO₂ + NIQ (Fig. 24 and Table S7†). Major deformation occurs when $h\nu$ passed to SIQPNO₂ with DOS of FP, pyz, and NIQ else it would have obtained a straight line due to structural stability. The SIQPNO₂ might have caused a mild permittivity to photocatalytically reduce MB in 190 min, unlike SIQPs with NIQ in 64 min (Tables 5 and 6). The DOS in NIQ could have been equilibrated w.r.t. each interacting site.

HR-TEM analysis

The HR-TEM image of IQPs and SIQPNO₂ on transmitting the electrons through a sample has produced the image with high-resolution 2D plane geometry (Fig. 25). SIQPNO₂ compared to IQPs indicates its unoptimized structure requiring 190 min to align for the PCR of the effluents of wastewater like MB (Fig. 25). The NIQ, CIQ, and SIQPNO₂ extended Schrodinger PE well due to the bonding of -NO₂, -Cl, and -NO₂ with asymmetric wavefunctions, unlike IQ. The smart quantum mechanics of IQ unlike others has acted as an ideal PE box of the Schrodinger equation performing PCR in 2 min. The HR-TEM image infers a linear pattern of IQ in one plane, expeditiously capturing the $h\nu$ s with the same wavefunctions (Fig. 25).

TGA

TGA on gradually raising the temperature exciting electrons of π and σ bonds caused weight loss as unstable components lost weight plotted against temperature (K_T) at specific frequency (ν) with $E = kK_T$, $E = h\nu$ or $E = \frac{hc}{\lambda}$ or $kK_T = h\nu$ for $\nu = \frac{kK_T}{h}$, where k is the Boltzmann distribution constant, K_T is the Kelvin T constant, h is the Planck constant, and E is the energy. The ν

value of weight loss at K_T elucidates the thermal stability of the molecules as onset weight loss. IQ lost weight as a single sharper peak at 290 °C with a rate of weight loss 350 $\mu\text{g min}^{-1}$ with ψ_1 (Fig. 26). While the NIQ and CIQ both have developed by destructively lowering a Φ where the IQ has acted as an excellent photocatalyst. NIQ has weight loss rate 425 $\mu\text{g min}^{-1}$ at ~ 350 °C due to asymmetric oscillations caused by NO₂. The NIQ slightly resists the electronic activities of NO₂ disrupting an overall crystallinity by delocalization. The CIQ destabilizes a crystallinity with rate of weight loss 325 $\mu\text{g min}^{-1}$ at ~ 290 °C with different FRET and hybridized $|\psi^2|$ (Fig. 26 and S25†). Two energies equilibrated as a straight line of weight loss from 200 to 300 °C with slope = 0. However, a few endothermic sharp changes appeared at 120 °C, followed by exothermic changes at 125 °C, attributed to the presence of benzene ring. It is accompanied by a slightly endothermic shoulder at 120 °C, due to O matching with the N cavity. After 300–800 °C, the closely placed oscillating peak with wavefunctions of each unit withdraw the intense changes. NIQ with SIQPI has transformed sharply into a multi-peak curve on sharing the electrons of NIQ. The molecule broadens a peak due to fused electron clouds. The CCA could have synchronised the SIQPI interactions with NIQ on broadening the peaks due to weaker FRET. The resulting electron clouds are differently reoriented as 1st order instead of 2nd for SIQPI with NIQ. The SIQPI with NIQ as 1st order TGA at a higher temperature on mutual activation of electron clouds at 20 $\mu\text{g min}^{-1}$ at ~ 300 °C than 400 $\mu\text{g min}^{-1}$ at ~ 230 °C with SIQPI alone (Fig S25†). Therefore, NIQ has enhanced the thermal stability of SIQPI by shortening a PCR time due to robust mutual resonating activity. NIQ with SIQPs expeditiously developed a FRET due to moderate electrostatic interactions lowering the weight loss without transition except for a single-crystal lattice as a novel eutectic mechanism. The SIQPs with anodic NIQ have shortened MB as cathodic PCR by 1.5, 1.2, and



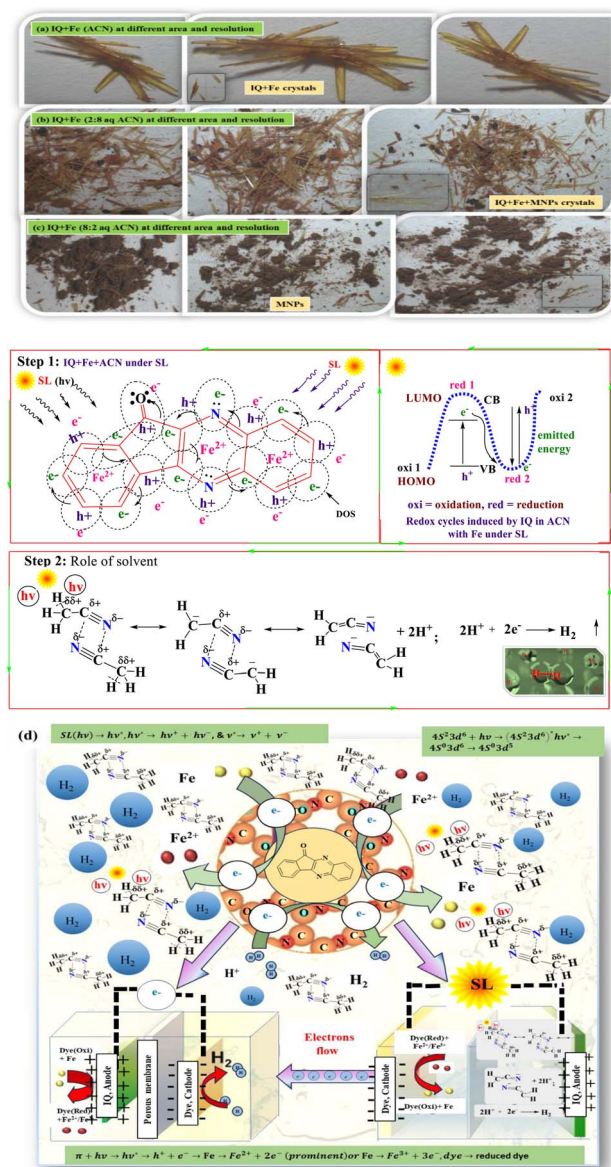


Fig. 30 Stereomicroscopic images of (a) IQ + Fe in ACN, forming crystals (b) IQ + Fe in 3 : 7 aq : ACN forming crystals, (c) IQ + Fe 7 : 3 aq : ACN forming MNPs, and (d) elucidates π -conjugation potential of IQ to oxidised Fe²⁺ and Fe³⁺ (and dyes) that nucleate the IQ in continuity to grow robust crystals.

1.1 times compared to SIQPs alone (Table 6). NIQ with ERG/OME of SIQPIII has disintegrated the electron cloud of the resulting framework.

SEM, stereomicroscopy, elemental analysis, single-crystal XRD, FT-IR spectroscopy, and UV-vis spectroscopy

IQ, a sharper nanorod unlike others with EWG and ERG has gained least organized edged morphology (Fig. 27). A polar solvent, ACN, has monodispersed IQ to align the crystals. The CIQ with Cl⁻ and >O coulombic linkages developed a linear crystal analyzed using a stereomicroscope (Fig. 28). Its crystallization could be catalyzed with a suitable solvent. However, IQ

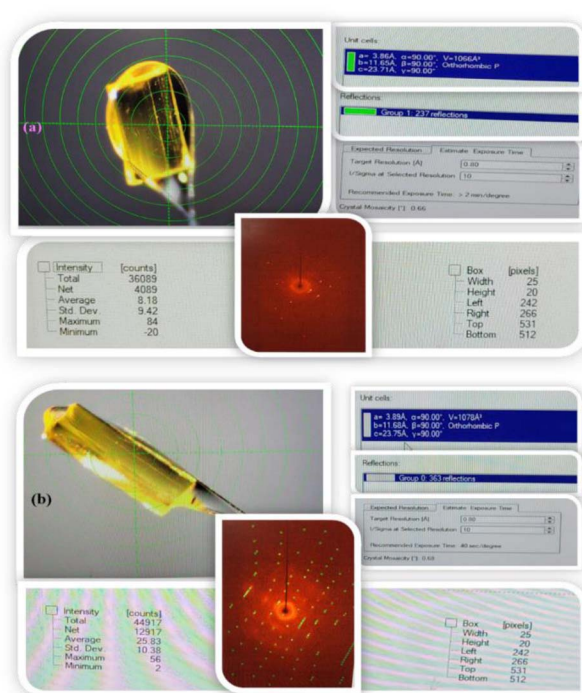


Fig. 31 IQ developed a sharp single crystal with Fe in (a) 3 : 7 aq : ACN and (b) 100% ACN.

with Fe scrap in ACN has nucleated a single crystal growing as sharp-edged nanorods along the walls of the vial while 9 : 1 aq : ACN has rusted out (Fig. 29 and 30).

Single-crystal XRD. IQ with 1.199 g Fe scrap of 2 cm length and 0.1 cm width in 5 mL ACN, placed in a closed vial for 2 weeks, has nucleated a single crystal of orthorhombic, space group (P) = 1, a = 3.86, b = 11.65, c = 23.71 Å and α = β = γ = 90° with 1066 (Å)³ (Fig. 30(a-d)). The crystal has mosaicity at 0.66–0.68° with 0.80 Å. The dipoles of water and ACN aligned along IQ to grow sharper single crystals in solution and along the wall unlike within 3 weeks in EtOH and CH₃OH separately reported elsewhere.⁴⁶ $\pi \rightarrow \pi^*$ and $n \rightarrow n^*$ of IQ with Fe split water with least E_a for nucleation with can, unlike with EtOH and CH₃OH, has elongated the nucleation time to 3 weeks due to higher solubility. The Fe scrap with IQ has nucleated sharper lattices in a shorter time, by replacing EtOH and CH₃OH by ACN.⁴⁶ However, the IQ in ACN with ionic interactions is linked with the Fe ion of scrap and ACN. However, IQ alone in ACN without scrap with least density has increased the vapour pressure by developing longer spikes than those of IQ with Fe in ACN remaining in the solution. The spikes and nanorods were developed along the wall due to vapor pressure. ACN has catalyzed IQ to form crystals with Fe linearly and oriented towards vapor sticking to walls on adhesion. IQ with Fe has formed crystals linearly and oriented towards vapor sticking to walls with adhesion in the ACN solvent. The spikes and nanorods were developed along the wall and aligned crystals. IQ grew sharp crystals and could act as smart electronics in emerging areas such as fingerprint and optoelectronics. Fe scrap with a larger surface area has weakened dipolar interactions of

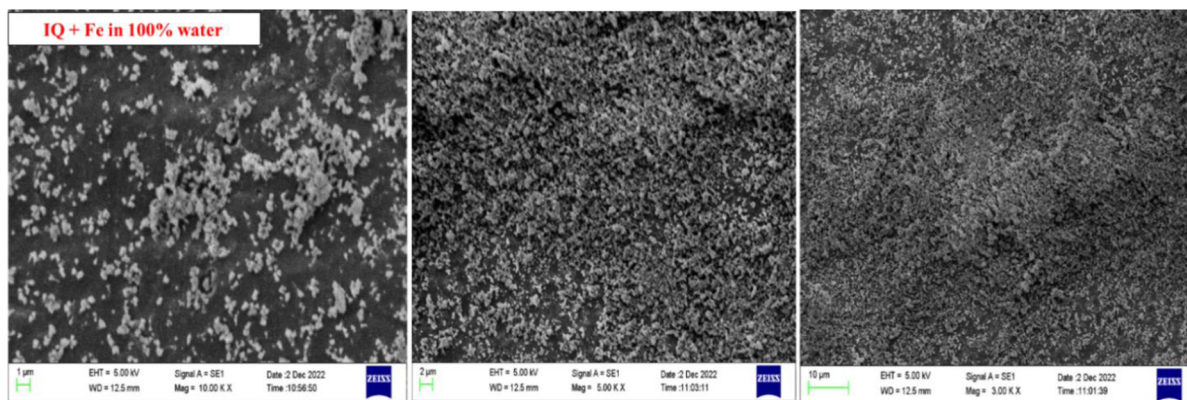


Fig. 32 SEM images of IQ + Fe in water.

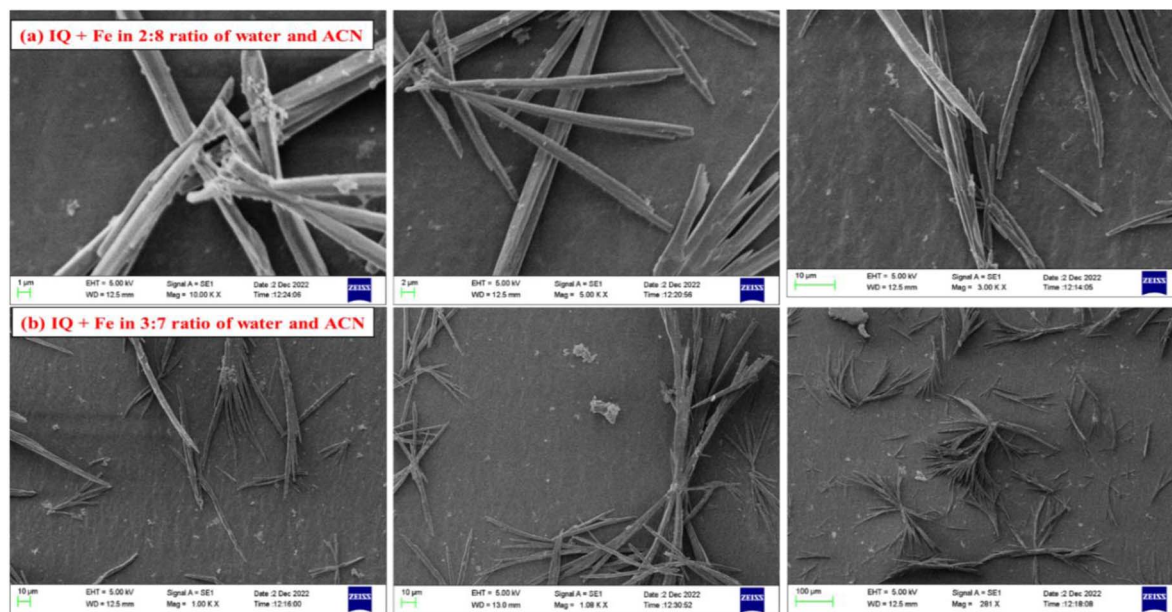


Fig. 33 SEM images of IQ + Fe in (a) 2 : 8 and (b) 3 : 7 solvent ratios of aq : ACN.

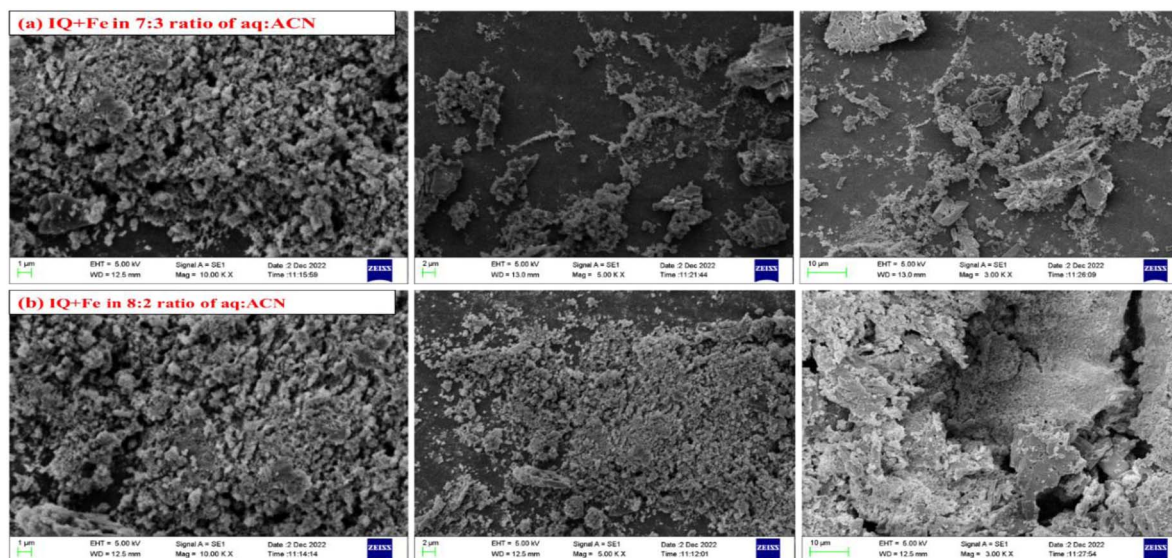


Fig. 34 SEM images of IQ + Fe in (a) 7 : 3 and (b) 8 : 2 aq : ACN solvent.



Table 7 Cutting edge for MNPs synthesis over conventional methods

Sr no.	Conventional methods	Ours methods
1	Excess NaOH is used	No
2	Heating	Under SL
3	Multiple washings	No
4	Multistep with manifolds infrastructure	×
5	Multistep process	Single step process
6	Specific pH	<i>In situ</i>
7	Specific temperature	Under SL at NTP
8	Trouble in getting desired particle size & shape	Not needed
9	Manifolds centrifuge	Not needed
10	Autoclaving	—

solvents for carrying IQ with Fe along the walls generating a metallic pressure. The Fe^{2+} and Fe^{3+} ions out of the Fe scrap could have aligned IQ linearly at surfaces to crystallize along the wall, interacting with oppositely charged sites of IQ as active *in situ* ROCs. The adequate $h\nu$ has sharpened a redox process of IQ with Fe catalyzing the nucleation and photoluminescence (Fig. 30 and 31). However, the sharper IR stretching indicates that FeO , Fe_2O_3 , and Fe_3O_4 and hydroxides have developed with IQ + Fe in aq : ACN, analysed by FT-IR spectroscopy, TGA, XRD, UV-Vis spectroscopy, and EDX (Fig. S26(b) and S27–S30†). Moreover, Fe with IQ has formed MNPs in 5 : 5 aq : ACN characterized by XRD and SEM (Fig. 32–34).

IQ with Fe scrap for versatile recycling: single crystals, MNPs, and for recovery of HIn from QHIn

IQ oxidizes the Fe scrap to develop the MNPs without co- or post-precipitation that eliminated a washing during synthesis (Table 7). The conventional methods trigger uncontrolled molecular and ionic activities during MNP synthesis along with other complications.⁴⁷ Therefore, the MNPs required washing with excess amounts of solvents and the infrastructure was then deleted with our recycling Fe scrap by the IQ photocatalyst method (Table S8†). The MNP synthesis conventionally⁴⁷ with FeSO_4 and FeCl_3 using excess NaOH require purification while the smart IQ photocatalyst has selectively responded to Fe scrap. However, the IQ with Fe has developed a single crystal in ACN unlike the MNPs in 5 : 5 of aq : ACN. The IQ catalyses the Fe scrap to generate the eigenenergies for developing MNPs without using salts as their removal complicates the process. Moreover, it has simplified and advanced the synthesis of MNPs by using renewable resources (SL) not reported yet. The XRD planes shown in Fig. 35 confirm the crystalline MNP formation with diffraction peaks at the (220), (311), (400), (511), and (440) lattice planes. The characteristic peak 311 at $2\theta = 37^\circ$ confirm a magnetite phase within the MNPs matching with the standard XRD data of magnetite⁴⁸ (Fig. 35).

Moreover, IQ with Fe scrap has reduced QHIn to HIn in nanoseconds while without Fe scrap in 17 min. The IQ catalyses

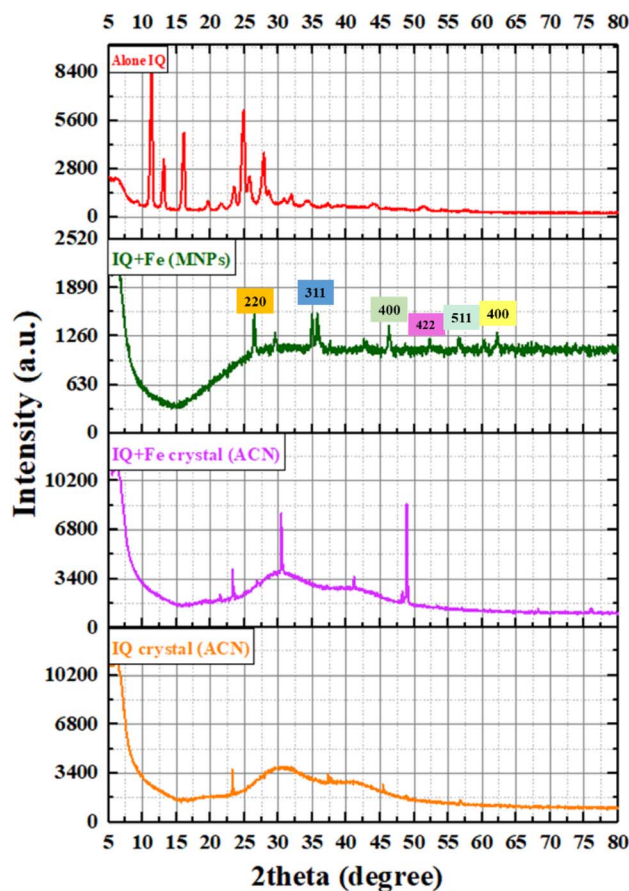


Fig. 35 XRD characterisation curve for IQ crystal, IQ + Fe crystal, MNPs, and alone IQ.

the Fe oxidation photocatalytically at NTP that reduced QHIn. Since inception, the HIn dye is used as an indicator in volumetric acid and base titrations and is drained out causing enormous pollution. Till date there are no remedial measures for degrading the persistent pollutant like QHIn, but IQ with Fe scrap has degraded that could further be extended to other pollutants and transition metals such as V, Cr, Mn, and Co scrap. The electrons released by Fe catalyse the reduction of

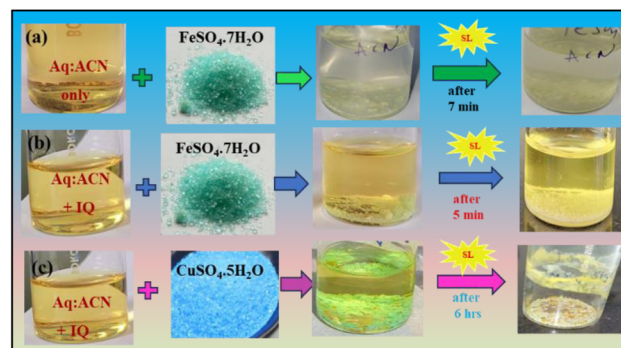


Fig. 36 (a) Alone aq : ACN solvent study with $\text{FeSO}_4 \cdot 7\text{H}_2\text{O}$ (b) IQ in aq : ACN with FeSO_4 , and (c) IQ in aq : ACN with $\text{CuSO}_4 \cdot 5\text{H}_2\text{O}$ formed nano thin film under SL.

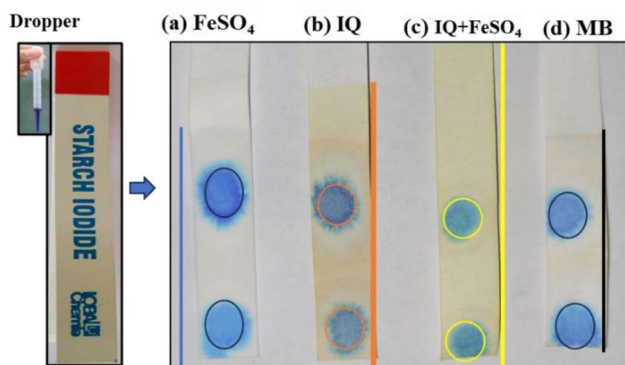


Fig. 37 Starch-iodide paper detect the absence of oxidizing agents. (a) MB + FeSO₄ on starch paper. (b) MB + IQ on starch paper. (c) MB + IQ + FeSO₄ on starch paper. (d) Only MB on starch paper.

QHIn by IQ, and similarly, they could reduce other persistent pollutants. Till date, no photocatalyst is reported that can advance the 1st and 2nd oxidations like Fe²⁺ and Fe³⁺ carried out by IQ to photocatalytically reduce a dye along with developing the MNPs. The same has been supported on FeSO₄ hydrolysis in 5 min with IQ unlike 7 min in aq : ACN under SL. The crystalline water was engaged by ACN *via* H dipolar interactions that cause the release of crystalline water from FeSO₄, whereas hydrolysis without IQ takes time; however, IQ has reduced the Fe and formed metal hydroxide with release of H₂ gas. However, CuSO₄ · 5H₂O with IQ took 6 h to decolourise blue copper to colourless and has formed homogeneous thin nano films at the glass vial walls under SL.

The 1st oxidation state of copper is highly stable due to its stable configuration; therefore, IQ dominantly split water and reduced copper. Since, IQ has developed dipolar-dipolar interactions with the medium and copper, forming a nano thin film at walls of the vials (Fig. 36). However, the solvent system catalyses the mechanism of nano monolayer thin film formation with IQ and fitted as per the Freundlich and Langmuir isotherm theory unlike metal remains at the bottom surface. In the same sequence, the starch iodide paper used with the solvent (aq : ACN) alone, FeSO₄, IQ, and IQ + FeSO₄ with MB drop strain (Fig. 37). IQ + FeSO₄ effectively reduced MB as the IQ and Fe have a strong interaction that has photocatalyzed MB with the highest rate as compared to solvent alone, FeSO₄ or IQ alone. This process can be applied for various metal extraction processes with IQ. Hence, IQ with its active configuration has undergone a robust transition that has split water (step 2) to oxygen and -OH.⁴⁹ The Fe with IQ has further catalysed a process as Fe → Fe²⁺ + 2e⁻ that reduces O₂ + 2e⁻ → O²⁻ and O²⁻ transfers its electron to water received from HO⁻ (step 3) to generate the holes by IQ on receiving the *hν*.

Mechanism

- Step 1: SL (*hν*) + IQ → IQ* → IQ* ≈ h⁺ + e⁻;
 Step 2: H₂O → H⁺ + HO⁻ (autosplit); HO⁻ → O²⁻ + H⁺;
 Step 3: SL (*hν*) + H₂O → 2H⁺ + HO⁻; 2O²⁻ + 4h⁺ → O₂;
 Step 4: Fe²⁺ + 2HO⁻ → Fe(OH)₂ → 2FeO + 2H₂O;
 Fe³⁺ + 3HO⁻ → Fe(OH)₃ → Fe₂O₃ + 3H₂O.



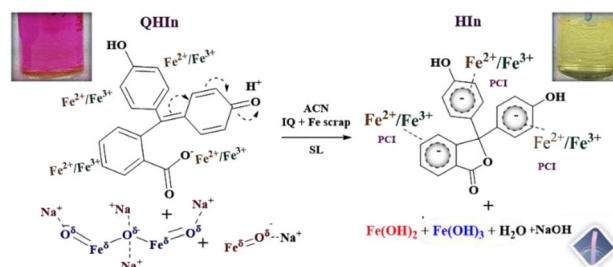
Fig. 38 Effect in degassed and distilled water on rusting with Fe scrap.

The same experiment was continued in degassed and distilled water where a degassed water has mildly rusted due to less dissolved O₂ (Fig. 38, S31, Tables 7 and S8†). The IQ with Fe scrap has expeditiously developed an anti-rusting sharp lattice in ACN reducing QHIn in seconds (Fig. 39). The IQPs and SIQPs having N atom, LPE, and π conjugated rings enhanced dye PCR. The intense yellow colour of IQ in aq-ACN with scrap has transition as follows: Fe → Fe²⁺ + 2e⁻ and Fe → Fe³⁺ + 3e⁻. The Fe²⁺ & Fe³⁺ both have initiated the π cationic interactions interfacing IQ with aligned wavefunctions of MNPs (Fig. 40). The Fe converted dissolved oxygen to O²⁻ producing (HO⁻) Fe₂O₃ as a major product (step 3) *in situ*, with different heat capacities. The Fe²⁺ formed O²⁻ *in situ* developing the oxides at the surfaces. The O²⁻ sticks to Fe²⁺ surfaces reducing water to (HO⁻) in a two-step process.

The 1st step is Fe → Fe²⁺ and the 2nd forms a product on reducing the negative charges indirectly. The Fe²⁺ and Fe³⁺ both reduce a dissolved oxygen to O²⁻ evolving the bubbles to surfaces as water approaches Fe²⁺/Fe³⁺ (Fig. S32†). This has reduced to HO⁻ on reacting with Fe²⁺/Fe³⁺ anodic reactions. The Fe²⁺/Fe³⁺ reacts to O²⁻/HO⁻ forming hydroxides with variable chemical rates. The IQ with Fe has reduced QHIn to HIn in seconds. The electrons of IQ *via* ROCs have formed crystals with metal (step 5).⁵⁰

Mechanism

- Step 1: SL (*hν*) + IQ + Fe (scrap) → IQ* → (IQ* ≈ h⁺ + e⁻);
 Step 2: IQ* + Fe (scrap) → Fe²⁺ + Fe³⁺; NaOH (*hν*) → Na⁺ + HO⁻;
 Step 3: H₂O (*hν*) → H⁺ + HO⁻; HO⁻ → O²⁻ + H⁺;
 2H⁺ + 2e⁻ → H₂↑;
 Step 4: Fe²⁺ + 2HO⁻ → Fe(OH)₂; Fe³⁺ + 3HO⁻ → Fe(OH)₃
 Step 5:



This mechanism elucidates the -OH formation as O atoms with partially negative charges engage Na⁺ as Fe²⁺ and Fe³⁺ align along O⁻ of the carboxyl group in QHIn (step 5). The resulting solution has yielded a white-colored HIn precipitate confirming with aq NaOH that had restored its pink color (Fig. S33†).

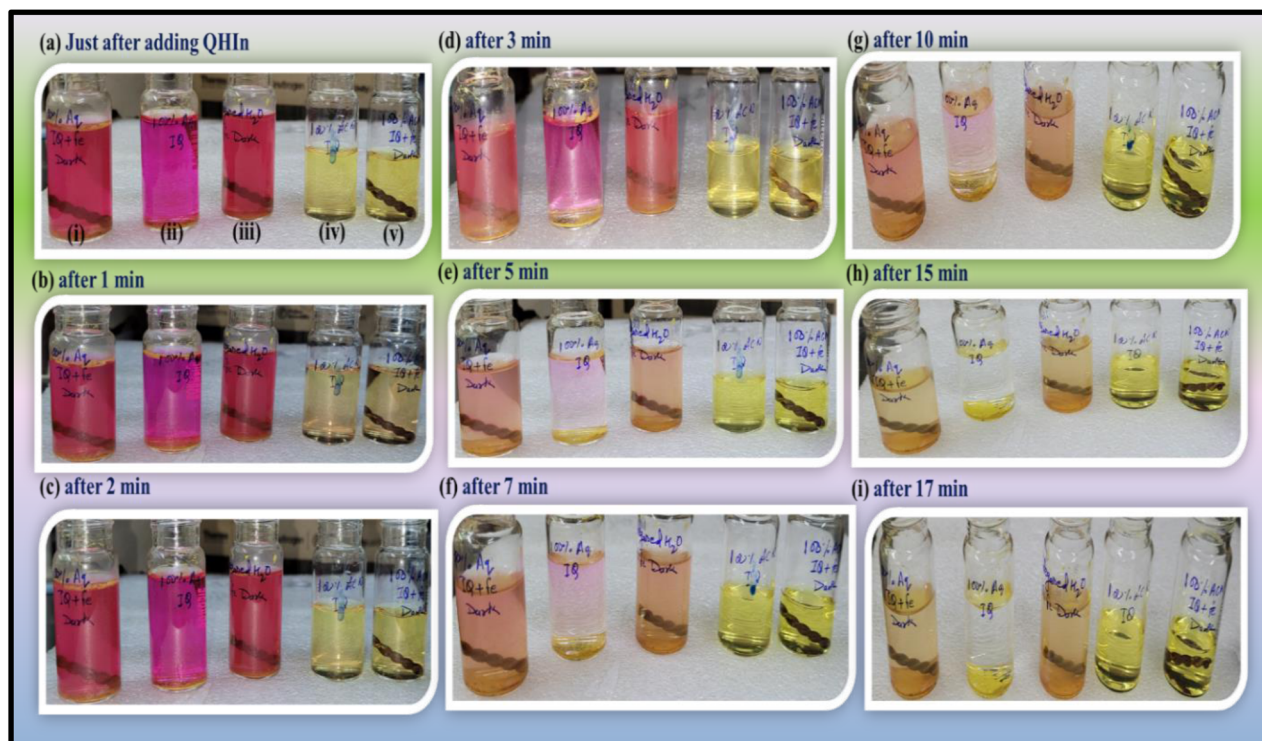


Fig. 39 Images of (i) IQ + Fe in aq, (ii) aq IQ only, (iii) IQ + Fe in degassed water, (iv) IQ in ACN, (v) IQ + Fe in ACN (a) initial and after (b) 1, (c) 2, (d) 3, (e) 5, (f) 7, (g) 10, (h) 15, and (i) 17 min.

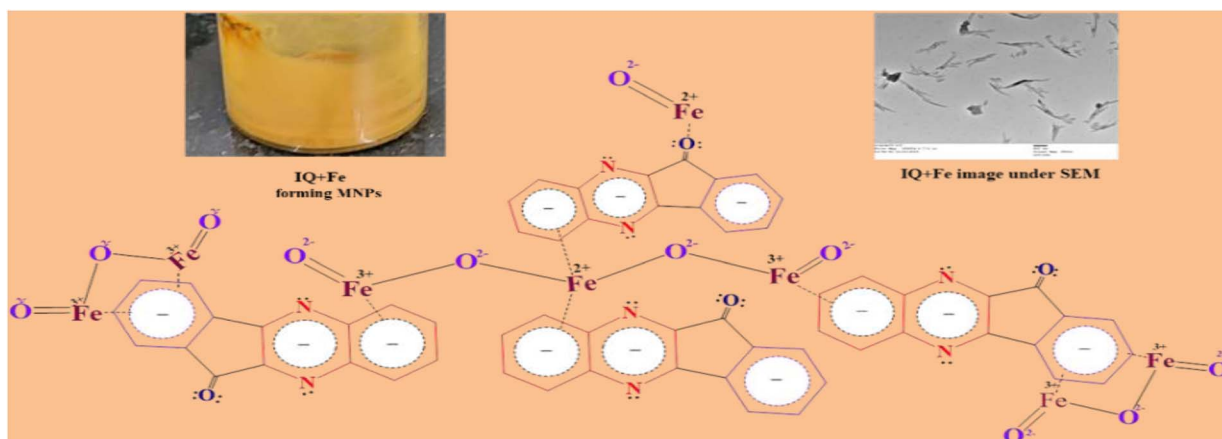


Fig. 40 Recycling mechanism of Fe scrap with IQ to develop MNPs in 5 : 5 aq : ACN.

The recovery of dyes from effluents has enhanced a novelty of IQ. While IQ with ACN has developed a single crystal as no oxygen was dissolved unlike the ratios 1 : 9, 2 : 8, 5 : 5, 7 : 3, and 8 : 2 of aq : ACN to oxidize Fe to MNPs (Chart S1†). The dipolar ACN has trapped $h\nu$ and detained SL partially forming metal oxides. Furthermore, aq-ACN has dissolved oxygen, further increasing with water %, leading to rusting. However, distilled and degassed water resulted in least rusting, depicting the oxidizing role of dissolved oxygen. ACN without dissolved oxygen acted as an anti-rusting agent in conjugation with IQ (Table S9†). The O^{2-} may affect the dipoles of ACN to catalyse oxygen ionization. The Fe reacted with dissolved O_2 where a subsequent interaction for rusting depends on increasing or decreasing the ratio of water with ACN. However, iodine with -0.54 V reduction potential could realign a delocalized IQ *vis-à-vis* Fe oxidation by substituting the presence of O^{2-} with quantized activities. The Fe metal framework has more affinity to bind I_2 than starch detecting the presence of Fe ions in IQ organometallic frameworks. It was found that 0.001 M IQ has degraded a 0.5 mL waste mobil oil with 1/50 ratio in 15 days with 3 : 7 aq : ACN of 0 mJ m^{-2} interfacial energies (Fig. S34 and Table S9†).

The IQ with robust FRET has disintegrated a waste mobil oil into fragments of shorter alkyl chains splitting waste hydrocarbons. The SIQPs in an alkaline medium reduced QHIn to HIn while IQ reduced mobil oil that was dispersed in an eluting solvent. It was monitored by TLC and stained with iodine and visualized under UV-Vis light. However, hexane : EA eluting solvent has widened IQ dispersion and degraded mobil oil salting out quasi-static adhesion on TLC. The mobil oil has developed a velocity gradient *in situ* with different retention factor (R_f) values. The eluting solvent hexane : EA has comparatively covered a maximum R_f value (Fig. S35†). Moreover, IQ breaks a longer C–C alkyl chain of oil into an alkene of shorter carbon chain with H_2 gas *via* a free radical disintegration mechanism. The IQ as reference upconversion nanomaterial and quantum mechanical sensor disintegrated the saturated hydrocarbons.^{51,52} IQ produced single-valued wavefunction of integrated π conjugated DOS as a quantum dot including antifungal activities by inhibiting fungal growth. The ACN with hydrophobicity has tuned interaction with host on increasing water concentration that might have blocked its reacting sites (Fig. S35†). The IQ could not interact and resulted in fungal activities. The explorative synergistic effects with other antifungal agents are being pursued in laboratory.⁵³ Moreover, IQ has effectively detached a dye from textile dyed fabric and the experiments are pursued in various aqueous waste solvent systems (Fig. S36†).

Conclusion

SIQPNO₂ has been synthesised with 85–90% and IQPs with 80–89% yields in ACN. The SIQPNO₂ and IQP photocatalysts photocatalytically reduced the pollutant MB, MO, BBR, and RhB dyes under SL in 2 to 87 min. The ERG of CIQ lowered PCR Φ unlike EWG of NIQ causing the different reorientations. IQ with waste Fe has developed robust MNPs in 5 : 5 aq : ACN, recovered

HIn, and developed a single crystal. SIQPNO₂ with two peripheral EWG NO₂ photocatalytically reduced MB in 190 than 2–32 min with IQPs. SIQPNO₂ alone has reduced MB in 2.16 times shorter period than with LaGT, acting as anti-PCR due to $4f^{ff}$. The rate of reaction, minimum energy, E_a , Φ , and photocatalytic activities were calculated from UV-Vis and fluorescence. Fe scrap in ACN had catalysed IQ to nucleate a single crystal as nanorods on recycling a waste metal. IQ with 100% ACN acted as an anti-rusting agent while with water has developed MNPs. The IQPs and SIQPNO₂ have reduced MB, MO, BBR, and RhB in a shorter time than with LaGT, TbGT, HoGT, and CeGT, as antireduction agents. IQPs and SIQPNO₂ could be extended to adsorb several toxic heavy metals from industrial effluents. These photocatalysts have reduced and physisorbed the industrial waste dyes, pollutants, and inks and were not photodegraded during the PCR process even after 5th run. Reducing dyes with IQPs and SIQPNO₂ is a sustainable separation with high Φ and could be substituted with EWG (SO₄) and ERG (NH₂) constitutional units for PCR. The studies are being pursued with other dyes such as naphthalene derivatives, persistent pollutants, and industrial wastes (used industrial wastes such as ink and oil). IQPs may quench ozone preventing holes and ROS in a free radical scavenging process.

Data availability

The following files are available free of charge *i.e.*, spectral data of ¹H, ¹³C NMR, FT-IR, XRD (powder), LC-MS, UV-Vis, EDX, and TGA spectra of all compounds (ESI†).

Conflicts of interest

The authors declare no competing financial interests.

Acknowledgements

The authors are thankful to the Central University of Gujarat, India for infrastructural support, UGC DAE CSIR Indore for Raman spectroscopy, and XRD single crystal for IIT Gandhinagar.

Notes and references

- 1 N. Shahrestani, F. Salahi, N. Tavakoli, K. Jadidi, M. Hamzehloueian and B. Notash, Asymmetric synthesis approach of enantiomerically pure spiro-indenoquinoxaline pyrrolidines and spiro-indenoquinoxaline pyrrolizidines, *Tetrahedron: Asymmetry*, 2015, **26**(20), 1117–1129, DOI: [10.1016/j.tetasy.2015.08.013](https://doi.org/10.1016/j.tetasy.2015.08.013).
- 2 N. Kumar, C. Lal, B. Singh and A. K. Patel, Synthesis and Biological Activities of Some Novel Spiro Heterocyclic Pyrrolizidine Derivatives of 11H-indeno[1,2-b]quinoxaline through 1,3-Dipolar Cycloaddition, *Asian J. Chem.*, 2020, **32**(5), 1255–1258, DOI: [10.14233/ajchem.2020.22630](https://doi.org/10.14233/ajchem.2020.22630).
- 3 R. Kumari and M. Singh, Spiroheterocyclic Photocatalyst for Reducing QHIn-Persistent Pollutants, Dyes, and Transition-



- Metal Ions Cocatalyzed with Electrolytes, *ACS Omega*, 2022, 7(44), 40203–40229, DOI: [10.1021/acsomega.2c05103](https://doi.org/10.1021/acsomega.2c05103).
- 4 S. R. Pandya and M. Singh, Dispersion and optical activities of newly synthesized magnetic nanoparticles with organic acids and dendrimers in DMSO studied with UV/vis spectrophotometry, *J. Mol. Liq.*, 2015, **211**, 146–156, DOI: [10.1016/j.molliq.2015.06.068](https://doi.org/10.1016/j.molliq.2015.06.068).
 - 5 S. Dev and M. Singh, Metallic sulfide nanoparticles anchored graphene oxide: Synthesis, characterization and reduction of methylene blue to leuco methylene blue in aqueous mixtures, *J. Phys. Chem. Solids*, 2020, **139**, 109335, DOI: [10.1016/j.jpcs.2020.109335](https://doi.org/10.1016/j.jpcs.2020.109335).
 - 6 J. Liu and Y. Lu, FRET Study of a Trifluorophore-Labeled DNzyme, *J. Am. Chem. Soc.*, 2002, **124**(51), 15208–15216, DOI: [10.1021/ja027647z](https://doi.org/10.1021/ja027647z).
 - 7 A. G. Naikwade, M. B. Jagdale, D. P. Kale, A. D. Gophane, K. M. Garadkar and G. S. Rashinkar, Photocatalytic Degradation of Methyl Orange by Magnetically Retrievable Supported Ionic Liquid Phase Photocatalyst, *ACS Omega*, 2020, **5**(1), 131–144, DOI: [10.1021/acsomega.9b02040](https://doi.org/10.1021/acsomega.9b02040).
 - 8 A. S. Yusuff, L. Taofeek Popoola and E. I. Aderibigbe, Solar photocatalytic degradation of organic pollutants in textile industry wastewater by ZnO/pumice composite photocatalyst, *J. Environ. Chem. Eng.*, 2020, **8**(4), 103907, DOI: [10.1016/j.jece.2020.103907](https://doi.org/10.1016/j.jece.2020.103907).
 - 9 L.-L. Tan, W.-J. Ong, S.-P. Chai and A. Rahman Mohamed, Reduced graphene oxide-TiO₂ nanocomposite as a promising visible-light-active photocatalyst for the conversion of carbon dioxide, *Nanoscale Res. Lett.*, 2013, **8**, 465, DOI: [10.1186/1556-276X-8-465](https://doi.org/10.1186/1556-276X-8-465).
 - 10 A. Salama, A. Mohamed, N. M. Aboamera, T. A. Osman and A. Khattab, Photocatalytic degradation of organic dyes using composite nanofibers under UV irradiation, *Appl. Nanosci.*, 2018, **8**, 155–161, DOI: [10.1007/s13204-018-0660-9](https://doi.org/10.1007/s13204-018-0660-9).
 - 11 S. Cailotto, *et al.*, Carbon dots as photocatalysts for organic synthesis: Metal-free methylene-oxygen-bond photocleavage, *Green Chem.*, 2020, **22**(4), 1145–1149, DOI: [10.1039/C9GC03811F](https://doi.org/10.1039/C9GC03811F).
 - 12 Y. Huang, Y.-X. Huang, J. Sun and C.-G. Yan, A [3+2] cycloaddition reaction for the synthesis of spiro[indoline-3,3'-pyrrolidines] and evaluation of cytotoxicity towards cancer cells, *New J. Chem.*, 2019, **43**(23), 8903–8910, DOI: [10.1039/C9NJ00994A](https://doi.org/10.1039/C9NJ00994A).
 - 13 A. L. Jadhav and G. D. Yadav, Clean synthesis of benzylidenemalononitrile by Knoevenagel condensation of benzaldehyde and malononitrile: effect of combustion fuel on activity and selectivity of Ti-hydroxalcite and Zn-hydroxalcite catalysts, *J. Chem. Sci.*, 2019, **131**(8), 79, DOI: [10.1007/s12039-019-1641-6](https://doi.org/10.1007/s12039-019-1641-6).
 - 14 M. Singh and R. Kumari, Correction to 'Photocatalytic Reduction of Fluorescent Dyes in Sunlight by Newly Synthesized Spiroindenoquinoxaline Pyrrolizidines', *ACS Omega*, 2020, **5**(36), 23201–23218, DOI: [10.1021/acsomega.0c05835](https://doi.org/10.1021/acsomega.0c05835).
 - 15 A. Suresh, T. V. Baiju, T. Kumar and I. N. N. Namboothiri, Synthesis of Spiro- and Fused Heterocycles via (4+4) Annulation of Sulfonylphthalide with o-Hydroxystyrenyl Derivatives, *J. Org. Chem.*, 2019, **84**(6), 3158–3168, DOI: [10.1021/acs.joc.8b03039](https://doi.org/10.1021/acs.joc.8b03039).
 - 16 K. Kumar, R. P. Dave, S. Dev and M. Singh, Study of molar properties of GO after doping with transition metals for photodegradation of fluorescent dyes, *RSC Adv.*, 2022, **12**(46), 29734–29756, DOI: [10.1039/d2ra04230d](https://doi.org/10.1039/d2ra04230d).
 - 17 G. A. Eldeken, F. A. El-Samahy, E. M. Zayed, F. H. Osman and G. E. H. Elgemeie, Synthesis, Biological Activities and Molecular Docking analysis of a Novel Series of 11H-Indeno[1,2-b]quinoxalin-11-one Derivatives, *J. Mol. Struct.*, 2022, **1261**, 132929, DOI: [10.1016/J.MOLSTRUC.2022.132929](https://doi.org/10.1016/J.MOLSTRUC.2022.132929).
 - 18 R. Kumari and M. Singh, Photocatalytic reduction of fluorescent dyes in sunlight by newly synthesized spiroindenoquinoxaline pyrrolizidines, *ACS Omega*, 2020, **5**(36), 23201–23218, DOI: [10.1021/acsomega.0c02976](https://doi.org/10.1021/acsomega.0c02976).
 - 19 C. T. Campbell, The Degree of Rate Control: A Powerful Tool for Catalysis Research, *ACS Catal.*, 2017, **7**(4), 2770–2779, DOI: [10.1021/acscatal.7b00115](https://doi.org/10.1021/acscatal.7b00115).
 - 20 Q. Yusen and E. J. Schelter, Lanthanide Photocatalysis, *Acc. Chem. Res.*, 2018, **51**(11), 2926–2936, DOI: [10.1021/acs.accounts.8b00336](https://doi.org/10.1021/acs.accounts.8b00336).
 - 21 J. Lavergne and W. Junge, Proton release during the redox cycle of the water oxidase, *Photosynth. Res.*, 1993, **38**, 279–296, DOI: [10.1007/BF00046752](https://doi.org/10.1007/BF00046752).
 - 22 D. Bouhafs, A. Moussi, A. Chikouche and J. M. Ruiz, Design and simulation of antireflection coating systems for optoelectronic devices: Application to silicon solar cells, *Sol. Energy Mater. Sol. Cells*, 1998, **52**(1–2), 79–93, DOI: [10.1016/S0927-0248\(97\)00273-0](https://doi.org/10.1016/S0927-0248(97)00273-0).
 - 23 A. K. Jangid, P. Malik and M. Singh, Mineral acid monitored physicochemical studies of oil-in-water nanoemulsions, *J. Mol. Liq.*, 2018, **259**, 439–452, DOI: [10.1016/j.molliq.2018.03.005](https://doi.org/10.1016/j.molliq.2018.03.005).
 - 24 J. Kou, C. Lu, J. Wang, Y. Chen, Z. Xu and R. S. Varma, Selectivity Enhancement in Heterogeneous Photocatalytic Transformations, *Chem. Rev.*, 2017, **117**(3), 1445–1514, DOI: [10.1021/acs.chemrev.6b00396](https://doi.org/10.1021/acs.chemrev.6b00396).
 - 25 L. A. Kurfman, T. T. Odbadrakh and G. C. Shields, Calculating Reliable Gibbs Free Energies for Formation of Gas-Phase Clusters that Are Critical for Atmospheric Chemistry: (H₂SO₄)₃, *J. Phys. Chem. A*, 2021, **125**(15), 3169–3176, DOI: [10.1021/acs.jpca.1c00872](https://doi.org/10.1021/acs.jpca.1c00872).
 - 26 H. De Raedt, Product formula algorithms for solving the time dependent Schrödinger equation, *Comput. Phys. Rep.*, 1987, **7**(1), 1–72, DOI: [10.1016/0167-7977\(87\)90002-5](https://doi.org/10.1016/0167-7977(87)90002-5).
 - 27 M. Bawin and A. Burnel, Single-valuedness of wavefunctions from global gauge invariance in two-dimensional quantum mechanics, *J. Phys. A: Math. Gen.*, 1985, **18**(11), 212, DOI: [10.1088/0305-4470/18/11/033](https://doi.org/10.1088/0305-4470/18/11/033).
 - 28 G. Ch. Mellau, Rovibrational eigenenergy structure of the [H,C,N] molecular system, *J. Chem. Phys.*, 2011, **134**, 194302, DOI: [10.1063/1.3590026](https://doi.org/10.1063/1.3590026).
 - 29 U. Hillmann, W. Schimmack, P. Jacob and K. Bunzl, In situ γ -spectrometry several years after deposition of radiocesium, *Radiat. Environ. Biophys.*, 1996, **35**, 297–303, DOI: [10.1007/s004110050043](https://doi.org/10.1007/s004110050043).



- 30 J. M. Cortina, J. P. Green, K. R. Keeler and R. J. Vandenberg, Degrees of Freedom in SEM: Are We Testing the Models That We Claim to Test?, *Organ. Res. Methods*, 2016, **20**(3), 350–378, DOI: [10.1177/1094428116676345](https://doi.org/10.1177/1094428116676345).
- 31 L.-Q. Chen, Chemical potential and Gibbs free energy II: Q&A, *MRS Bull.*, 2022, **47**(8), 753–758, DOI: [10.1557/s43577-022-00405-3](https://doi.org/10.1557/s43577-022-00405-3).
- 32 P. Dais, Impact of Gibbs' and Duhem's approaches to thermodynamics on the development of chemical thermodynamics, *Arch. Hydrobiol. Suppl.*, 2021, **75**(2), 175–248, DOI: [10.1007/s00407-020-00259-8](https://doi.org/10.1007/s00407-020-00259-8).
- 33 G. G. Láng, Basic interfacial thermodynamics and related mathematical background, *ChemTexts*, 2015, **1**, 16, DOI: [10.1007/s40828-015-0015-z](https://doi.org/10.1007/s40828-015-0015-z).
- 34 J. Zhu, Z. Zhu, H. Zhang and S. Küppers, Enhanced photocatalytic activity of Cedoped Zn-Al multi-metal oxide composites derived from layered double hydroxide precursors, *J. Colloid Interface Sci.*, 2016, **481**, 144–157, DOI: [10.1016/j.jcis.2016.07.051](https://doi.org/10.1016/j.jcis.2016.07.051).
- 35 M. H. Elsayed, T. M. Elmorsi, A. M. Abuelela, A. E. Hassan, A. Z. Alhakemy, M. F. Bakr and H. H. Chou, Direct sunlight-active Na-doped ZnO photocatalyst for the mineralization of organic pollutants at different pH mediums, *J. Taiwan Inst. Chem. Eng.*, 2020, **115**, 187–197, DOI: [10.1016/j.jtice.2020.10.018](https://doi.org/10.1016/j.jtice.2020.10.018).
- 36 J. M. Lee, S. B. Yuk, J. W. Namgoong and J. P. Kim, Mechanofluorochromism of Triphenylamine-BODIPY: Effect of twisted intramolecular charge transfer and restriction in rotation on fluorescence, *Dyes Pigm.*, 2021, **185**(Part A), 108864, DOI: [10.1016/j.dyepig.2020.108864](https://doi.org/10.1016/j.dyepig.2020.108864).
- 37 E. J. Sie, Observation of Exciton Redshift-Blueshift Crossover in Monolayer WS₂, *Nano Lett.*, 2017, **17**, 4210–4216, DOI: [10.1021/acs.nanolett.7b01034](https://doi.org/10.1021/acs.nanolett.7b01034).
- 38 S. Calati, Q. Li, X. Zhu and G. Stahler, Ultrafast evolution of the complex dielectric function of monolayer WS₂ after photoexcitation, *Phys. Chem. Chem. Phys.*, 2021, **23**, 22640–22646, DOI: [10.1039/D1CP03437E](https://doi.org/10.1039/D1CP03437E).
- 39 R. Salzwedel, A. Knorr, D. Hoeing, H. Lange and M. Selig, Theory of radial oscillations in metal nanoparticles driven by optically induced electron density gradients, *J. Chem. Phys.*, 2023, **158**(6), 064107, DOI: [10.1063/5.0139629](https://doi.org/10.1063/5.0139629).
- 40 M. Chandra, S. S. Indi and P. K. Das, Depolarized Hyper-Rayleigh Scattering from Copper Nanoparticles, *J. Phys. Chem. C*, 2007, **111**(28), 10652–10656, DOI: [10.1021/jp071847l](https://doi.org/10.1021/jp071847l).
- 41 K. Thakur and B. Kandasubramanian, Graphene and Graphene Oxide-Based Composites for Removal of Organic Pollutants: A Review, *J. Chem. Eng. Data*, 2019, **64**(3), 833–867, DOI: [10.1021/acs.jced.8b01057](https://doi.org/10.1021/acs.jced.8b01057).
- 42 J. M. Garcia, L. F. Heald, R. E. Shaffer and S. G. Sayres, Oscillation in Excited State Lifetimes with Size of Sub-nanometer Neutral (TiO₂)_n Clusters Observed with Ultrafast Pump–Probe Spectroscopy, *J. Phys. Chem. Lett.*, 2021, **12**(16), 4098–4103, DOI: [10.1021/acs.jpclett.1c00840](https://doi.org/10.1021/acs.jpclett.1c00840).
- 43 M. Hosni, Y. Kusumawati, S. Farhat, N. Jouini and Th. Pauporté, Effects of Oxide Nanoparticle Size and Shape on Electronic Structure, Charge Transport, and Recombination in Dye-Sensitized Solar Cell Photoelectrodes, *J. Phys. Chem. C*, 2014, **118**(30), 16791–16798, DOI: [10.1021/jp412772b](https://doi.org/10.1021/jp412772b).
- 44 A. Fujishima, X. Zhang and D. A. Tryk, *Surf. Sci. Rep.*, 2008, **63**, 515–582, DOI: [10.1016/j.surfrep.2008.10.001](https://doi.org/10.1016/j.surfrep.2008.10.001).
- 45 Z. A. Piskulich, O. O. Mesele and W. H. Thompson, Activation Energies and Beyond, *J. Phys. Chem. A*, 2019, **123**(33), 7185–7194, DOI: [10.1021/acs.jpca.9b03967](https://doi.org/10.1021/acs.jpca.9b03967).
- 46 N. Elangovan and S. Sowrirajan, Synthesis, single crystal (XRD), Hirshfeld surface analysis, computational study (DFT) and molecular docking studies of (E)-4-((2-hydroxy-3,5-diiodobenzylidene)amino)-N-(pyrimidine-2-yl) benzenesulfonamide, *Heliyon*, 2021, **7**(8), e07724, DOI: [10.1016/j.heliyon.2021.e07724](https://doi.org/10.1016/j.heliyon.2021.e07724).
- 47 P. Biehl, M. von der Lüh, S. Dutz and F. H. Schacher, Synthesis, Characterization, and Applications of Magnetic Nanoparticles Featuring Polyzwitterionic Coatings, *Polymers*, 2018, **10**, 91, DOI: [10.3390/polym10010091](https://doi.org/10.3390/polym10010091).
- 48 J. Sun, S. Zhou, P. Hou, Y. Yang, J. Weng, X. Li and M. Li, Synthesis and characterization of biocompatible Fe₃O₄ nanoparticles, *J. Biomed. Mater. Res.*, 2006, **80A**, 333–341, DOI: [10.1002/jbm.a.30909](https://doi.org/10.1002/jbm.a.30909).
- 49 S. K. Sahoo, *et al.*, Photocatalytic Water Splitting Reaction Catalyzed by Ion-Exchanged Salts of Potassium Poly(heptazine imide) 2D Materials, *J. Phys. Chem. C*, 2021, **125**(25), 13749–13758, DOI: [10.1021/acs.jpcc.1c03947](https://doi.org/10.1021/acs.jpcc.1c03947).
- 50 C. T. Campbell, The Degree of Rate Control: A Powerful Tool for Catalysis Research, *ACS Catalysis*, 2017, **7**(4), 2770–2779, DOI: [10.1021/acscatal.7b00115](https://doi.org/10.1021/acscatal.7b00115).
- 51 A. Hemmati, H. Emadi and S. Reza Nabavi, Green Synthesis of Sulfur- and Nitrogen-Doped Carbon Quantum Dots for Determination of L-DOPA Using Fluorescence Spectroscopy and a Smartphone-Based Fluorimeter, *ACS Omega*, 2023, **8**(23), 20987–20999, DOI: [10.1021/acsomega.3c01795](https://doi.org/10.1021/acsomega.3c01795).
- 52 T. Naghdi, S. Faham, T. Mahmoudi, N. Pourreza, R. Ghavami and H. Golmohammadi, Phytochemicals toward Green (Bio) sensing, *ACS Sens.*, 2020, **5**(12), 3770–3805, DOI: [10.1021/acssensors.0c02101](https://doi.org/10.1021/acssensors.0c02101).
- 53 D. Makawana and M. Singh, A new dendrimer series: synthesis, free radical scavenging, and protein binding studies, *RSC Adv.*, 2020, **10**, 21914–21932, DOI: [10.1039/D0RA04102E](https://doi.org/10.1039/D0RA04102E).

